Simulation of the mineral dust emission frequencies from desert areas of China and Mongolia using an aerodynamic roughness length map derived from the POLDER/ADEOS 1 surface products

B. Laurent, B. Marticoréna, G. Bergametti, P. Chazette, F. Maignan, C. Schmechtig

Simulation of the mineral dust emission frequencies from desert areas of China and Mongolia using an aerodynamic roughness length map derived from the POLDER/ADEOS 1 surface products

B. Laurent, B. Marticorena, and G. Bergametti

Laboratoire Interuniversitaire des Systèmes Atmosphériques, Universités Paris VII-XII, UMR CNRS 7583, Créteil, France

P. Chazette and F. Maignan

Laboratoire des Sciences du Climat et de l'Environnement, Commissariat à l'Energie Atomique, UMR CNRS 1572, Saclay, France

C. Schmechtig

Laboratoire Interuniversitaire des Systèmes Atmosphériques, Universités Paris VII-XII, UMR CNRS 7583, Créteil, France

Received 14 May 2004; revised 19 August 2004; accepted 22 November 2004; published 1 April 2005.

[1] To determine the location of the potential dust source regions and to evaluate the dust emission frequencies over the arid and semiarid areas of China and Mongolia (35.5°N–47°N; 73°E–125°E), we established a map of Z_0 from the composition of protrusion coefficient (PC) derived from the POLDER-1 bidirectional reflectance distribution function (BRDF). Using a $^1/_4° \times {}^1/_4°$ resolution Z_0 data set, we derived a map of the 10-m erosion threshold wind velocity for the Chinese and Mongolian deserts. The retrieved erosion thresholds range from 7 m s^{-1} in the sandy deserts (Taklimakan, Badain Jaran, and Tengger deserts) to up to 20 m s^{-1} in the Gobi desert. They are comparable to the minimum wind velocity measured in meteorological stations during dust storms in the Taklimakan (6–8 m s^{-1}) and in the Gobi desert (11–20 m s^{-1}). These erosion thresholds were combined with surface wind fields, soil moisture, and snow cover to simulate the dust emission frequencies of the eastern Asian deserts over 3 years (1997–1999). The simulations point out the Taklimakan desert and the deserts of northern China as the most frequent sources of dust emissions. The simulated seasonal cycle is characterized by a maximum in late spring and a minimum in late autumn and winter. The comparison with climatologic studies of dust storms derived from synoptic observations confirms the importance of these two source areas and the reliability of the simulated seasonal cycle. It reveals an underestimation of the dust emission frequency in the Gobi desert, because of a low frequency of high wind velocities. Our results also suggest that soil moisture and snow cover are not the main factors controlling the seasonal cycle or the interannual variability of the dust emission frequencies. We finally compared the simulated dust event frequencies to occurrences of Total Ozone Mapping Spectrometer (TOMS) Absorbing Aerosol Index (AAI) higher than 0.7 over the Taklimakan desert, where mineral dust is expected to be the dominant absorbing aerosol. A very good agreement is obtained between the simulated frequencies and the TOMS AAI frequencies on monthly and seasonal timescales.

Citation: Laurent, B., B. Marticorena, G. Bergametti, P. Chazette, F. Maignan, and C. Schmechtig (2005), Simulation of the mineral dust emission frequencies from desert areas of China and Mongolia using an aerodynamic roughness length map derived from the POLDER/ADEOS 1 surface products, *J. Geophys. Res.*, *110*, D18S04, doi:10.1029/2004JD005013.

1. Introduction

[2] Mineral dust emitted by wind erosion is a major source of tropospheric aerosol. Indeed, the global quantity of mineral aerosol injected in the atmosphere is ~2150 Tg yr^{-1} [*Intergovernmental Panel on Climate Change*, 2001], i.e., about 40% of the global annual mass of aerosols emitted on Earth.

[3] Eastern Asian deserts appear as one of the main sources of deposition fluxes to the ocean [*Duce*, 1995]. Moreover, large areas of ongoing desertification due to land

0148-0227/05/2004JD005013$09.00

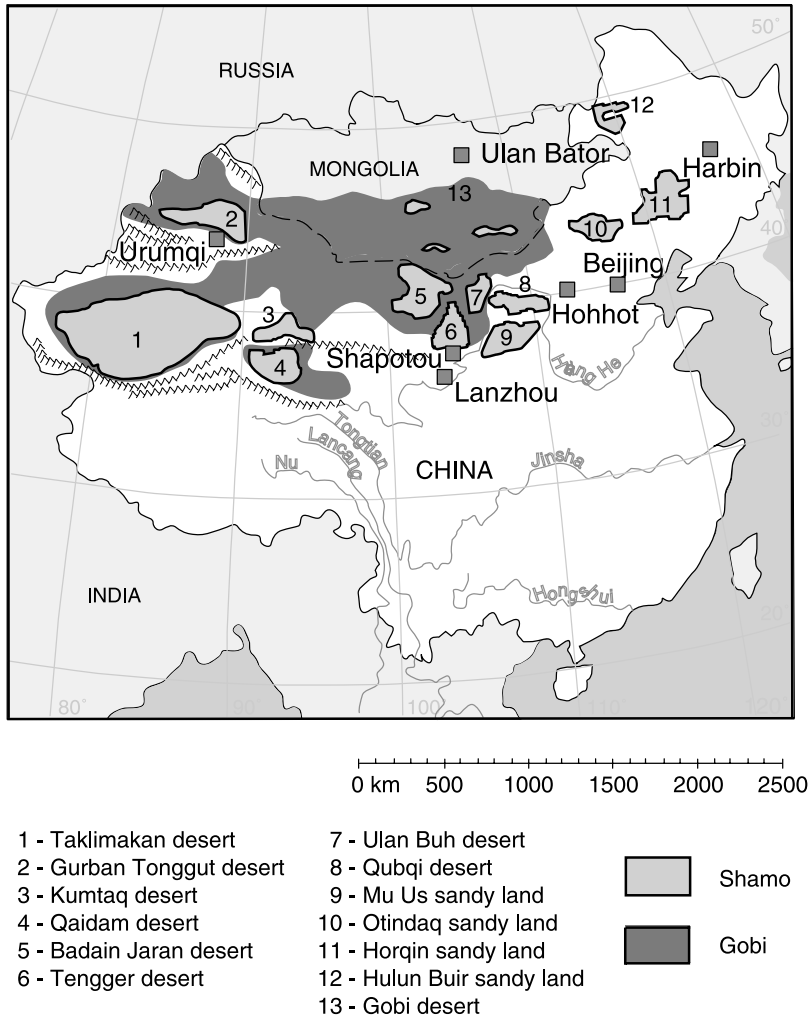

Figure 1. Desert and desertified areas in eastern Asia (adapted from *Mitchell and Fullen* [1994] and *Sun et al.* [2001]).

use have been identified in China [*Mainguet*, 1996; *Xue*, 1996; *Zha and Gao*, 1997] and in Mongolia [*Natsagdorj et al.*, 2003]. Current global and regional models generally failed in simulating the variability of the dust distribution in this region because of a poor spatial resolution and an inaccuracy in the description of the dust emissions [*Gong et al.*, 2003]. Detailed dust emission schemes have recently been included in regional model to simulate the mineral dust loading and its transport over China [*Gong et al.*, 2003] and also to forecast the occurrence of dust storm [*Shao et al.*, 2003]. The emission schemes used in these modeling studies [*Marticorena and Bergametti*, 1995; *Shao et al.*, 1996; *Alfaro and Gomes*, 2001; *Shao*, 2001] provide a physical description of the main processes involved in the dust production: the erosion threshold, the saltation fluxes and the aerosol production by sandblasting processes.

[4] The erosion threshold wind velocity is one of the key parameters to describe these emissions. In fact, the dust emission frequency is determined by the number of time the wind velocity exceeds the erosion threshold while the dust emission intensity depends on how much the threshold is exceeded. The erosion threshold is mainly controlled by the surface features (soil size distribution, surface roughness, soil moisture, etc.). However, little information is available on these surface features in arid regions and particularly on the surface roughness. More often, all the desert surfaces are described with the same surface roughness while the roughness length can range over 3 or 4 orders of magnitude in arid areas. For example, *Gong et al.* [2003] derived a surface roughness map from a detailed land use map with a high spatial resolution (1 km $\times$ 1 km) for which desert surfaces are only characterized by a unique land class. Similarly, *Shao et al.* [2003] only distinguished desert surfaces from vegetated areas.

[5] Recently, *Marticorena et al.* [2004] have investigated the possibility to retrieve the surface roughness of arid areas using the surface bidirectional reflectance products derived from passive multidirectional measurements in the solar spectrum of the Polarization and Directionality of the Earth Reflectance (POLDER-1) sensor. An empirical relationship between the aerodynamic roughness length and the so-called protrusion coefficient (PC) of the surface derived from the POLDER-1 bidirectional reflectance distribution function (BRDF) has been established and applied over the Sahara and the Arabian Peninsula.

[6] In the present study, we extend this approach to the Chinese and Mongolian deserts. The objective is to investigate the location of the most frequent sources of dust

emissions. Thus a composition of PC has been performed over the arid and semiarid lands of China and Mongolia allowing the derivation of an aerodynamic roughness length map. The retrieved roughness lengths have been used to assess the 10 m wind velocities at erosion threshold. The dust emission frequencies have been computed for 1997, 1998 and 1999 from these erosion thresholds and surface wind fields provided by the European Centre for Medium range Weather Forecasts (ECMWF, Reading, UK). The influence of soil moisture and snow cover on the dust emission frequencies has also been investigated. The results of the simulations are discussed and compared to climatology of dust storms available in the literature and to satellite observations.

2. Description of the Deserts of China and Mongolia and of the Dust Emission Patterns

[7] The main deserts and arid areas in eastern Asia are presented in Figure 1. They are mainly composed of sandy (referred to shamo) or stony surfaces (referred to gobi) and are identified as the principal source areas of dust emission of this region [*Sun et al.*, 2001]. In China, the desert areas represent 13.6% of the Chinese territory [*Sun et al.*, 2001], i.e., a bit less than 1.4 millions km^2, of which the Taklimakan, one of the largest sandy desert of the world, covers 272,000 km^2. The Gobi desert, which stretches over the south of Mongolia, the Inner Mongolia and the north of China, is characterized by stony surfaces and covers 1.05 millions km^2. The main deserts identified in China and Mongolia from the literature include both natural and desertified areas (n° 10, 11) [*Xue*, 1996; *Zha and Gao*, 1997]. Most of the sandy deserts are located in closed basins, surrounded by mountains. For instance, the Taklimakan desert corresponds to the closed basin of Tarim, the Gurban Tonggut desert stands on the basin of Junggaar, and the Badain Jaran and Tengger deserts both stand on the basin of Hanhai. As a result, most of these sandy deserts are surrounded by stony deserts. Such depressed locations can induce specific air circulations. The Tarim basin is surrounded in the north, the west and the south by mountains higher than 5000 m, the Kulun Mounts, and the near surface wind is northeasterly (except for the western margins) [*Sun*, 2002]. As a result, dust should remain confined in the southwestern slopes of the Kulun Mounts. However, dust emitted from the Taklimakan desert can be lifted to altitudes higher than 5000 m and transported by westerly jet stream for long distances. It is mainly due to the coupling of a cold high-pressure cell over the Taklimakan and a warm low-pressure cell over the Tibetan Plateau [*Sun*, 2002].

[8] Analyses of long-term synoptic measurements of dust storms and dust haze from meteorological stations allow assessing the long-term trend of the dust storm occurrence and the typical seasonal pattern of the mineral dust emissions in China and Mongolia. *Sun et al.* [2003] examined the variation of sand and dust storms occurrence from 1954 to 2001. They noticed a continuous decrease in the number of sand and dust storms from 1954 to the 1990s, but a slightly increase in 2000 and 2001. In Mongolia, *Natsagdorj et al.* [2003] noticed an increase in the number of dusty days from the 1960s (15 d yr^{-1}) to the 1980s (50 d yr^{-1}) but confirms a decrease between 1980 and 1999 (40 d yr^{-1}).

[9] The dust emissions exhibit a strong seasonal cycle characterized by a maximum in spring both in China and Mongolia [*Sun et al.*, 2001, 2003; *Natsagdorj et al.*, 2003], when the surface wind velocities are the highest and the precipitation are very low [*Parungo et al.*, 1994]. A secondary maximum can be observed during the fall in Mongolia [*Natsagdorj et al.*, 2003] or during winter (December and January) in the northern deserts of China [*Sun et al.*, 2003]. The seasonal variations of the frequency of dust storms are found significantly correlated with the frequency of strong winds (>6.5 m s^{-1}) [*Kurosaki and Mikami*, 2003]. In particular, the unusual increase of observed dust storms during the recent years (2000–2002) compared to the previous period (1993–1999) is explained by a higher occurrence of strong winds [*Kurosaki and Mikami*, 2003]. Thus these results suggest that the interannual variability of the dust outbreak frequency is mainly driven by the variability in the occurrence of strong winds. *Kurosaki and Mikami* [2004] also indicate that snow cover can have a significant influence on the dust storm frequency during the spring in eastern Asia.

[10] The minimum wind velocity measured in the meteorological stations during dust storms gives an indication on the erosion thresholds wind velocities. Such an approach was applied to the measurements from meteorological stations in Mongolia (including part of the Gobi desert) [*Natsagdorj et al.*, 2003] and in the Xinjiang province of China (including the Taklimakan and Gurban Tonggut deserts) [*Wang et al.*, 2003]. In the Gobi desert, dust storms are associated to wind velocities usually ranging from 11 to 20 m s^{-1} [*Natsagdorj et al.*, 2003], while in the Taklimakan desert they range from 6 to 8 m s^{-1} [*Wang et al.*, 2003]. These observations indicate that the erosion thresholds in eastern Asia vary significantly from one desert to another. Since the erosion threshold is mainly controlled by the surface roughness, this suggests that the variability of the surface roughness must be taken into account to correctly describe the dust storm frequency.

3. Mapping the Aerodynamic Roughness Length

[11] In order to cover most of the Chinese and Gobi deserts, we investigated the area located between 35.5°N to 47°N and 73°E to 125°E. The retrieval of roughness lengths was performed using the method described below and proposed by *Marticorena et al.* [2004]. A composite PC data set was established from an appropriate selection of POLDER-1 data.

3.1. POLDER-1 Surface Product

[12] POLDER-1 was a radiometer with a wide field of view (2400 × 1800 km^2) onboard the polar heliosynchronous ADEOS 1 platform. It provided global and systematic measurements of spectral, directional and polarized characteristics of the solar radiation which is reflected by the atmosphere, terrestrial surfaces, and oceans. POLDER-1 observed a same site under many geometries of observation (between 10 and 15 observations for each passage of the satellite) with viewing zenith angles up to about 60° for the full azimuth range. Its revisit period was almost daily with a

resolution on the ground at nadir of 6 × 7 km^2 for the ADEOS altitude of 800 km. It allows the composition of the BRDF within a 30-day period. In spite of its short-lived functioning (30 October 1996 to 30 June 1997), POLDER-1 provided a large set of measurements of surface reflectance, ρ, at three wavelengths in the visible range: 443, 670, and 865 nm.

[13] The surface POLDER-1 products are operationally geocoded and calibrated, and the cloudy pixels are flagged [*Leroy et al.*, 1997; *Hautecoeur and Leroy*, 1998]. The signal is corrected from the contributions of molecular scattering, absorbing gases (O_3, O_2, H_2O) and stratospheric aerosols, but the effects of tropospheric aerosols are not. Details of the processing for the surface products are given by *Leroy et al.* [1997].

3.2. Protrusion Coefficient and Aerodynamic Roughness Length

[14] The semiempirical model of *Roujean* [1991] is used in the POLDER-1 processing line to retrieve the BRDF. *Roujean* [1991] models the reflectance as a combination of both surface and volume components. A semiempirical relation of the bidirectional reflectance, ρ, is established for each wavelength [*Roujean et al.*, 1992]:

$$\rho(\theta_s, \theta_v, \phi) = k_0 + k_1.f_1(\theta_s, \theta_v, \phi) + k_2.f_2(\theta_s, \theta_v, \phi) \quad (1)$$

where θ_s and θ_v are respectively the Sun and viewing zenith angles, and f is the difference of azimuth angles between the Sun and the viewing directions. The surface (f_1) and volume (f_2) scattering functions have been derived from theoretical considerations, as described in *Roujean et al.* [1992, 1997]. Finally, the parameters k_0 (zenith reflectance), k_1 (surface diffusion) and k_2 (volume diffusion) are functions of surface properties:

$$k_0 = \rho_0\left(\alpha + (1-\alpha)e^{-bF}\right) + \frac{r}{3}\left(1 - e^{-bF}\right)(1-\alpha)$$

$$k_1 = \frac{hl}{S}\rho_0\alpha$$

$$k_2 = r\left(1 - e^{-bF}\right)(1-\alpha)$$

where

- ρ_0 background and protrusion reflectance;
- α relative weight of the volume and surface components;
- b an empirical constant;
- h average height of surface protrusion;
- l average length of surface protrusion;
- S horizontal surface associated with each protrusion;
- r facet reflectance;
- F facet area index (LAI in the case of a canopy).

[15] From the theoretical expressions of the k_i coefficients, *Roujean et al.* [1992] defined the dimensionless PC, characterizing the surface roughness:

$$PC = \frac{k_1}{k_0} \quad (2)$$

where k_0 and k_1 parameters are retrieved from the fitting of the BRDF model with the reflectances $\rho(\theta_s,\theta_v,\varphi)$ measured by POLDER-1 over 30 days.

[16] The PC has been compared to measurements or estimates of aerodynamic roughness lengths, Z_0, over various unvegetated desert areas (Sahara, North Africa; Namibia, South Africa; Death Valley, California) for a wide range of surface roughness [*Marticorena et al.*, 2004]. Marticorena et al. derived an empirical relationship allowing the estimation of Z_0 from PC:

$$Z_0 = a\exp\left(\frac{PC}{b}\right) \quad (3)$$

with $a = 4.859 \times 10^{-3}$ cm and $b = 0.052$ is dimensionless.

3.3. Data Set Composition

[17] As mentioned above, 8 months of POLDER-1 observations are available from November 1996 to June 1997. Since the surface roughness is expected to be constant over the arid desert regions, any time period of observation could be used to establish a PC data set. However, persistent cloud cover sometimes prevents the retrieval of the BRDF, even for a 30-day composition. In order to obtain a PC map as complete as possible, data sets for several months and two wavelengths (670 nm and 865 nm; note that because of inaccurate calibration, the near UV wavelength 443 nm was not used) have been used for the composition. Moreover, since no correction is performed in the POLDER-1 processing line for the possible effects of tropospheric aerosol, we limited the sampling period to winter months during which the dust emissions are known to be the lowest in eastern Asia [*Parungo et al.*, 1994; *Sun et al.*, 2001, 2003]. Finally, the PC composition map is based on 8 data sets corresponding to 4 months (November 1996 to February 1997) and 2 wavelengths.

[18] In order to increase the confidence level of the final composition, a selection of the monthly and composite data sets has been performed.

3.3.1. Selection

[19] The objective of the selection is to exclude from the composition the data for which the BRDF was not correctly modeled. This can result either from a low number of observations used for the fitting, or from the dispersion of the observations.

[20] Thus the first criterion for the data selection is a threshold on the number of observations used for the fitting of the BRDF. For the Sahara desert, *Marticorena et al.* [2004] estimated to 100 the minimal number of required observations to provide a good representativeness of the BRDF model. Since the sensor is the same and the type of surface is similar, we used the same number of observations as the minimum required to fit the BRDF for each pixel.

[21] The quality of the surface products obtained from POLDER-1 is quantified by a signal to noise ratio (SNR). If the effect of tropospheric aerosols becomes significant along the period during which the BRDF composition is made, the SNR of the directional signature should significantly degrade [*Hautecoeur and Leroy*, 1998]. Following *Marticorena et al.* [2004], we applied a threshold of 5 dB on the SNR to avoid such a possible contamination. Applying these criteria to the eight available data sets (4 months with

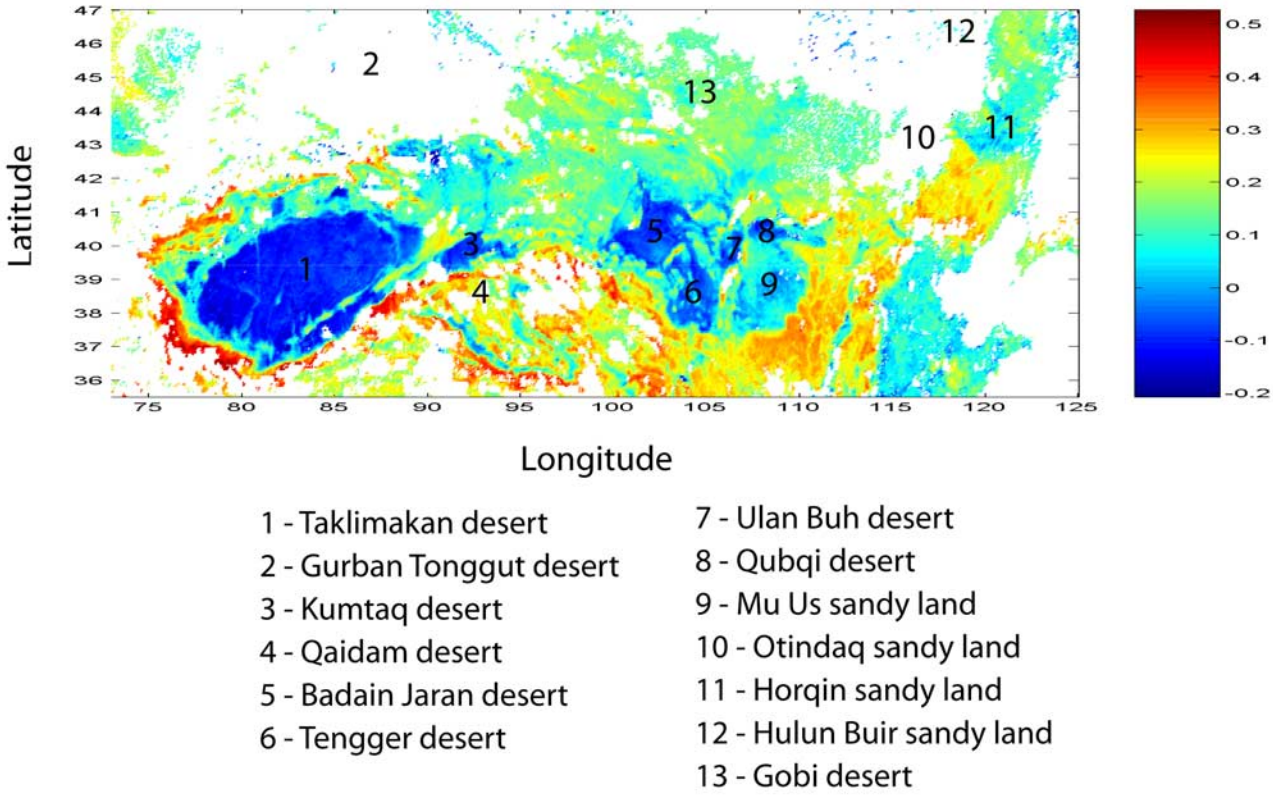

Figure 2. Nominal resolution composite map of PC derived from POLDER-1 BRDF.

two wavelengths each), the final set represents 603,057 data, i.e., 58% of the initial data.

3.3.2. PC Composition

[22] The initial composition consists in computing the median, PC, and the associated standard deviation, σ, from the selected monthly values. This procedure allows the computation of 104,416 medians, i.e., 104,416 different pixels are documented over the selected area.

[23] Over arid areas the surface roughness is expected to be constant, so σ should be very low. On the opposite, vegetated areas or surfaces temporarily covered by snow or water may exhibit some variability during the 4-month period. To select only stable surfaces, the PC monthly values which are not included in the interval defined by PC ± σ were excluded from the composition. To obtain a representative composite data set, we also rejected the cases for which less than 3 monthly data sets are available out of a maximum of 8. These two selections exclude 22% of data.

[24] The final PC composition presented in Figure 2 is made of 81,514 pixels. Despite the persistence of clouds and/or snow over some areas, especially in the northern part of the map, most of the deserts identified on Figure 1 are retrieved. This is the case for the deserts in the southern part of the studied area, i.e., the Taklimakan (1), Kumtaq (3), Quaidan (4), Badain Jaran (5), Tengger (6), Ulan Buh (7), Qubqi (8) and Mu Us (9) deserts. In the northeastern part, the Horqin sandy land (11) is retrieved, while the Otin Daq (10) and Hulun Buir (12) sandy lands are totally missing. The Gobi desert (13) is only partially retrieved, half of the pixels in the area defined by 42°N–47°N, 90°E–110°E being missing. In the northwestern part of the studied area, the Gurban Tonggut desert (2) is also totally missing.

[25] For the whole data set, PC values range from −0.32 to 0.53. The lower value corresponds to the smoother surfaces and the higher one corresponds to the rougher surfaces. The upper limit obtained for the Chinese and Gobi deserts (0.53) is higher than the one for the Sahara desert (0.35), while the lowest value (−0.32) is significantly lower than the one retrieved for the Sahara desert (of the order of −0.1) [*Marticorena et al.*, 2004]. The highest values are located in the mountains surrounding the Taklimakan and in the Tibetan Plateau. The differences with the highest values obtained in the Sahara desert could be explained by the fact that these mountains are steeper and more uneven. Concerning the lowest values, 14 pixels (among the 81,514 available) scattered on the map exhibit values below −0.20. The examination of the "Quick Look" Spot images for those pixels revealed water, snow or ice covered surfaces. Such surfaces can be retrieved because they are almost permanently covered by ice, snow or water. The retrieved PC are geophysically meaningful since such smooth surfaces should produce a strongly negative PC. However, since these surfaces are not relevant for dust emissions, these pixels have been discarded. Values lower than −0.15 located in the southwestern part of the Taklimakan are more numerous and will be discussed below.

3.4. Consistency of the PC Values

[26] The relevance of the information provided by the PC can hardly be directly assessed since very few roughness length measurements are available over the arid areas of the

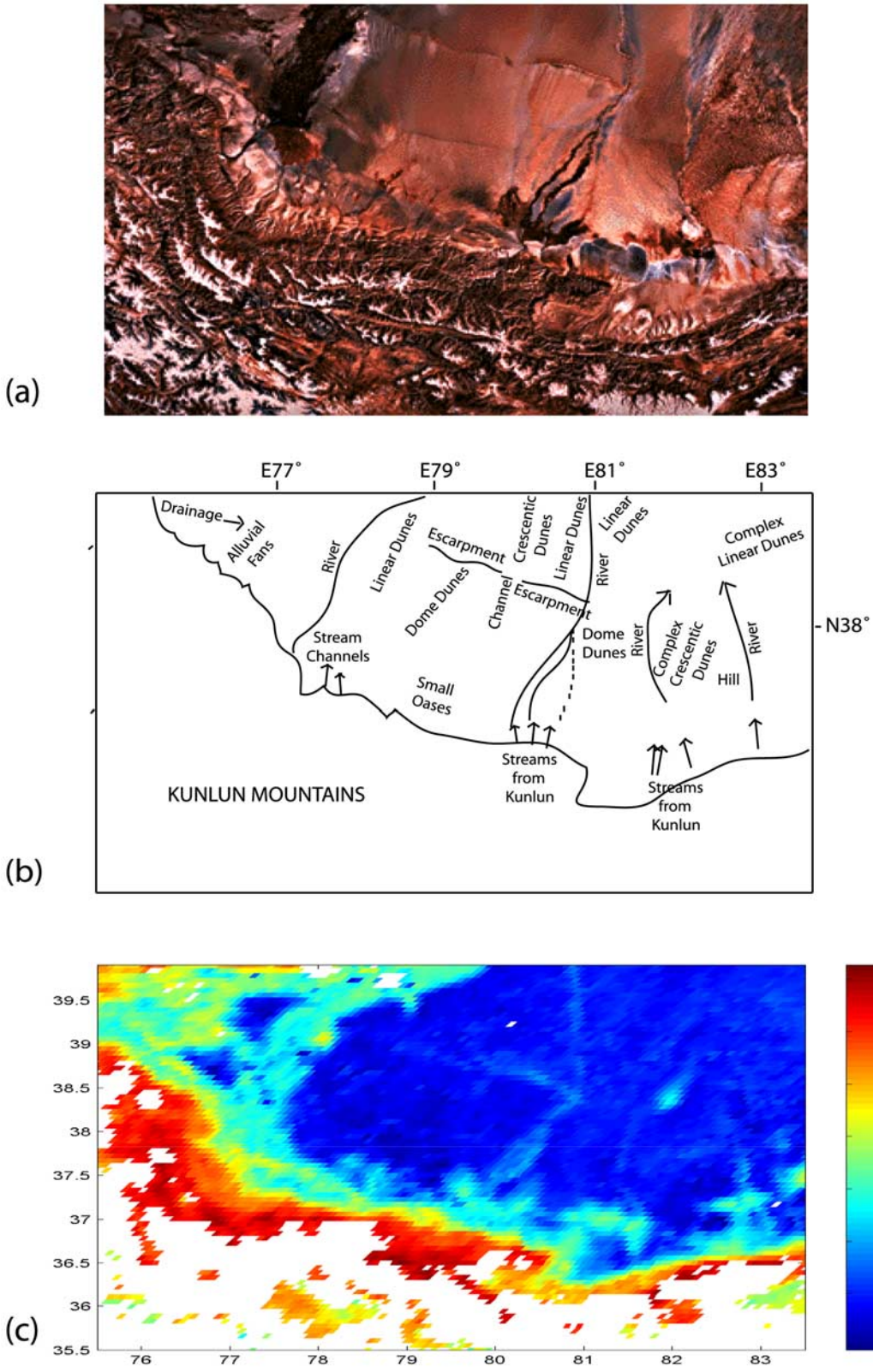

Figure 3. Comparison between (a) a high-resolution Landsat image from which is derived (b) a geomorphologic map and (c) a composite map of PC in the southwestern Taklimakan desert (Figures 3a and 3b derived from *Walker* [1986]).

Table 1. Median Protrusion Coefficient (PC) and Standard Deviation (σ) for Typical Surfaces of Chinese Arid and Semiarid Areas

Surface Type	Geographical Coordinates	PC	
		Median	σ
Mountain range (Kunlun Mounts)	36.8°N–37.6°N; 76°E–77°E	4.29E-01[a]	4.51E-02
Loess plateau	36.9°N–37.9°N; 109.5°E–110.5°E	3.21E-01	1.99E-02
Stony desert	41°N–43°N; 99°E–100°E	1.32E-01	3.18E-02
Stony desert	41°N–42°N; 91.5°E–92.5°E	1.03E-01	2.13E-02
Vegetated sandy land (Mu Us)	37.6°N–40°N; 107.7°E–109°E	4.78E-02	3.83E-02
Sand dunes(N-E Taklimakan)	39°N–40.5°N; 84°E–87°E	−8.87E-02	1.76E-02
Sand dunes with silty deposit (S-W Taklimakan)	37.7°N–38.7°N; 78.5°E–80.5°E	−1.32E-01	2.80E-02

[a]Read 4.29E-01 as 4.29×10^{-1}.

world. However, (1) the consistency of the PC for different surface types clearly identified from a geomorphologic point of view and (2) the consistency of the values for a given surface type in different locations can be examined.

[27] *Walker* [1986] provided a geomorphologic analysis of six Landsat images corresponding to typical desert surfaces of Chinese deserts: the Mu Us sandy land, the Tengger desert, the Turpan depression, the Lop Nur depression, the northeast Taklimakan desert and the southwest Taklimakan desert. Additional information on the spatial distribution of soil texture was found in the Soil Atlas of China [*Hseung*, 1986]. For the parts of the Landsat images where the composite PC map is complete enough, a direct visual comparison is allowed. The PC map is consistent with the Landsat images and their geomorphologic interpretation. The main geomorphologic structures and their locations, elements of relief, and streams are clearly identified on the composite PC map. An example of such a comparison is given in Figure 3 which corresponds to the southwestern part of the Taklimakan desert. On the PC map, the Kulun Mounts appear as having high PC values (rough surface) or as missing data (cloud and/or snow). Independently of their characteristics (linear or domes), the dune areas (sandy smooth surfaces) exhibit similar and very low PC. The stream channels and the escarpment identified on the Landsat image are also clearly visible on the PC map.

[28] A more quantitative validation has been performed by comparing the PC values obtained for the different types of surfaces identified by *Walker* [1986] or *Hseung* [1986]. Table 1 reports the median PC obtained for each of the surface types described. The rougher surfaces located in the mountain ranges surrounding the Taklimakan desert and in the Tibetan Plateau correspond to the highest PC. The sandy surfaces are characterized by low PC values.

[29] To test the consistency of the PC map, the variability of PC for given surface types was also examined. The sandy areas are the main surface type that can unambiguously be identified and located on the basis of the available documentation. We have thus determined the median PC for the main sandy areas of the Chinese deserts (Table 2). Almost all the identified sandy areas exhibit the same range of PC (−0.05 to −0.09) except for the Mu Us sandy land, the Horqin sandy land, and the southwestern part of the Taklimakan desert. The higher PC obtained for the Mu Us and for the Horqin sandy lands are consistent with the fact that these areas are partially vegetated [*Walker*, 1986] and thus rougher than bare sandy surfaces. The southwestern part of the Taklimakan exhibits lower PC values than the other sandy areas. As mentioned above (part 3.3.2.), this area is also identified as having much lower PC than the minimum value observed for the Sahara [*Marticorena et al.*, 2004]. Over smooth surfaces, such as sandy surfaces, the surface roughness is mainly induced by the soil structure and the roughness length can be roughly estimated as $^1/_{30}$ of the soil grains diameter (D_p) [*Greeley and Iversen*, 1985]. From this estimation, a finer soil texture is likely to exhibit a smoother surface. From equation (3), the lowest PC retrieved in the southwestern Taklimakan corresponds to roughness lengths ranging from 1.26×10^{-4} to 2.72×10^{-4} cm. Such roughness lengths can be produced by soil grain diameters from 37 to 82 μm. The Soil Atlas of China [*Hseung*, 1986] mentions alluvial deposits and sandy silts (4–63 μm) in this area which is consistent with these grain diameters. The existence of a particularly smooth surface induced by a fine textured soil in this area is thus highly probable.

3.5. Map of Aerodynamic Roughness Length

[30] The final composite map of the protrusion coefficient has the nominal resolution of the POLDER-1 pixel, i.e., 6×7 km^2 ($\sim^1/_{16}° \times {}^1/_{16}°$). This resolution is well adapted for mesoscale atmospheric transport models but too precise for

Table 2. Median Protrusion Coefficient (PC) and Standard Deviation (σ) for the Main Chinese Sandy Areas

Name	Geographical Coordinates	PC	
		Median	σ
Horqin	42.7°N–43.6°N; 120°E–121.5°E	5.65E-02	3.87E-02
Mu Us	37.5°N–39.5°N; 107°E–109°E	4.84E-02	3.88E-02
Tengger	38°N–39.5°N; 103.5°E–105.5°E	−4.92E-02	2.94E-02
Qubqi	40.1°N–40.7°N; 107.5°E–108.7°E	−5.36E-02	4.87E-02
Ulan Buh	39.5°N–40.3°N; 105.8°E–106.7°E	−5.64E-02	4.38E-02
Kuntaq	39.3°N–40°N; 91.3°E–92.3°E	−6.42E-02	4.76E-02
Badain Jaran	39.8°N–41.3°N; 101.5°E–103°E	−7.93E-02	2.91E-02
N-E Taklimakan	39°N–40.5°N; 84°E–87°E	−8.87E-02	1.76E-02
S-W Taklimakan	37.7°N–38.7°N; 78.5°E–80.5°E	−1.32E-01	2.80E-02

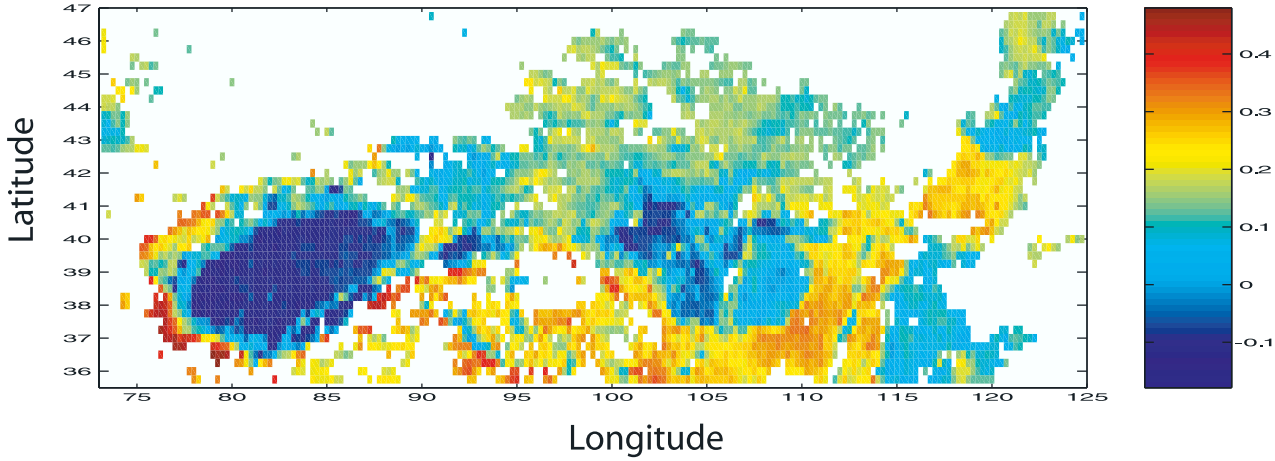

Figure 4. Map of PC at the spatial resolution of $^1/_4° \times {}^1/_4°$.

global-scale simulations. As an example, the DREAM regional model [*Nickovic et al.*, 2001] provided forecasts of the dust emissions with spatial resolutions of $^1/_{10}° \times {}^1/_{10}°$ or 0.3° × 0.3°, while *Tegen et al.* [2004] performed global simulations including a dust emission model with a spatial resolution of $^1/_2° \times {}^1/_2°$. *Marticorena et al.* [2004] have compared the frequency distribution of protrusion coefficients for maps with different spatial resolutions, from the nominal resolution of the POLDER-1 data up to a 1° × 1° resolution. Marticorena et al. showed that a decrease of the spatial resolution down to $^1/_4° \times {}^1/_4°$ does not introduce significant bias on the PC frequency distribution compared to the one retrieved from the nominal resolution data set. Similar tests have been performed for our composite data set and led to the same conclusion. An operational data set of PC is thus provided at the spatial resolution of $^1/_4° \times {}^1/_4°$ (Figure 4). It can be observed that compared to the nominal resolution map (Figure 2), the $^1/_4° \times {}^1/_4°$ map (Figure 4) preserves the main geomorphologic structures. The range of PC values of the $^1/_4° \times {}^1/_4°$ map (−0.18 to 0.48) is similar to the range for nominal resolution PC map (−0.20 to 0.53). The same ranges of values are found in the same locations and no false information is generated in the areas where there is no data.

[31] From this PC map at the spatial resolution of $^1/_4° \times {}^1/_4°$ and equation (3), we computed a map of the logarithm of the aerodynamic roughness length (Figure 5). The retrieved Z_0 values range from 1.5×10^{-4} cm to 0.3 cm for the different deserts. These values are comparable to the range of roughness lengths measured over natural erodible surface with a portable wind tunnel [*Gillette et al.*, 1982]: the lowest measured Z_0 is about 1×10^{-4} cm, while the maximum roughness length for which the erosion threshold has been reached is less than 0.5 cm. Table 3 presents the median Z_0 for selected homogeneous areas of the major deserts. Several categories of arid and semiarid areas can be identified from the rougher and less erodible surfaces to the smoothest ones. The stony deserts have the highest Z_0 (6.4×10^{-2} cm). Over the Gobi desert, 70% of the retrieved Z_0 range from 1.5×10^{-2} cm to 10^{-1} cm, while 30% range from 10^{-1} cm to 5×10^{-1} cm. This range of Z_0 is consistent with the Z_0 experimentally determined in the Death Valley (California) for unvegetated surfaces covered with gravel, cobbles, or boulders (7.6×10^{-2} cm < Z_0 < 3.47×10^{-1} cm) [*Greeley et al.*, 1997]. The partially vegetated sandy lands of Horqin and Mu Us have similar Z_0, respectively 1.3×10^{-2} cm and 1.2×10^{-2} cm, i.e., 1 order of magnitude higher than the other sandy deserts

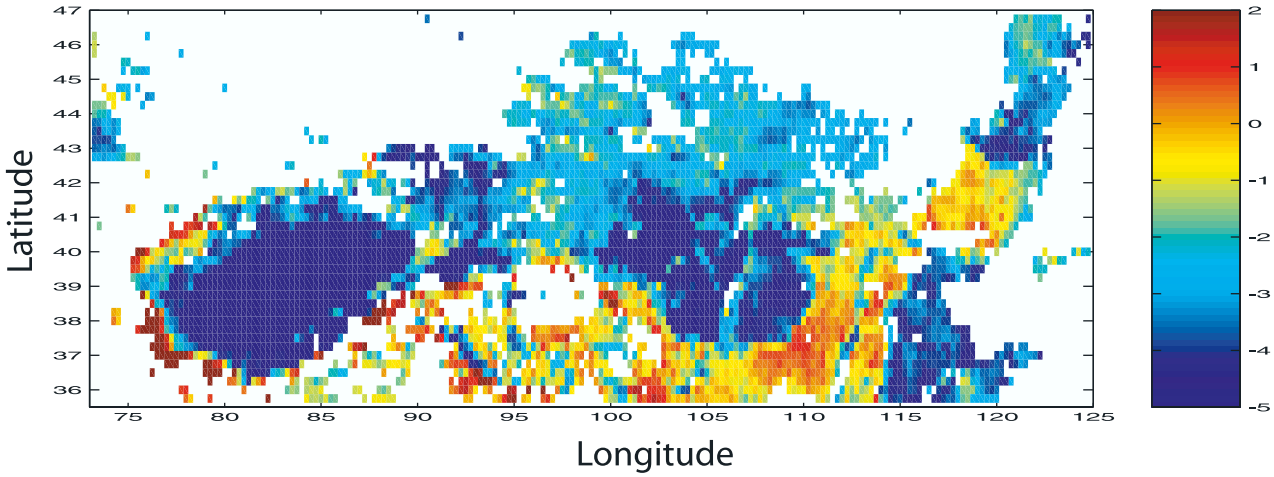

Figure 5. Map of the logarithm of the aerodynamic roughness length Z_0 with a spatial resolution of $^1/_4° \times {}^1/_4°$.

Table 3. Median Aerodynamic Roughness Length (Z_0) and Standard Deviation (σ) Derived From PC for the Main Arid Areas of Eastern Asia

		Z_0, cm	
Name	Geographical Coordinates	Median	σ
Stony desert	41°N–43°N; 99°E–100°E	6.42E-02	2.85E-02
Stony desert	41°N–42°N; 91.5°E–92.5°E	3.40E-02	9.60E-03
Horqin	42.7°N–43.6°N; 120°E–121.5°E	1.28E-02	6.30E-03
Mu Us	37.5°N–39.5°N; 107°E–109°E	1.23E-02	9.10E-03
Tengger	38°N–39.5°N; 103.5°E–105.5°E	2.20E-03	7.50E-03
Qubqi	40.1°N–40.7°N; 107.5°E–108.7°E	2.20E-03	5.20E-03
Ulan Buh	39.5°N–40.3°N; 105.8°E–106.7°E	1.70E-03	2.40E-03
Kuntaq	39.3°N–40°N; 91.3°E–92.3°E	1.30E-03	3.80E-03
Badain Jaran	39.8°N–41.3°N; 101.5°E–103°E	1.00E-03	9.68E-04
N-E Taklimakan	39°N–40.5°N; 84°E–87°E	8.72E-04	2.49E-04
S-W Taklimakan	37.7°N–38.7°N; 78.5°E–80.5°E	3.82E-04	3.31E-04

(Tengger, Qubqi, Ulan Buh, Kuntaq, Badain Jaran) whose Z_0 range from 2.2×10^{-3} cm to 1×10^{-3} cm. These values are comparable to the Z_0 experimentally determined for an interdunal area and desert flats in the Namib desert (4×10^{-3} cm and 4.2×10^{-2} cm) [*Greeley et al.*, 1997]. The southwestern part of the Taklimakan appears as the smoothest and thus the most erodible surface, with typical Z_0 lower than 10^{-3} cm. Such low values of roughness length have been measured in wind tunnel studies for homogeneous sand beds [*Li and Martz*, 1994; *McKenna-Neuman and Nickling*, 1994] but also for natural surfaces [*Gillette et al.*, 1982].

[32] The roughness lengths over the various arid areas of eastern Asia thus range at least over 3 or 4 orders of magnitude (from less than 10^{-3} cm in sandy areas of the Taklimakan up to 5×10^{-1} cm in some parts of the Gobi desert) suggesting very different erosion thresholds from one desert to another.

4. Dust Emission Frequencies

[33] Dust emissions depend on both the surface roughness and the soil size distribution [*Marticorena and Bergametti*, 1995; *Shao*, 2001]. The surface roughness mainly influences the erosion threshold and thus has a strong effect on the dust emission frequency [*Marticorena et al.*, 2004], while the rate of dust emission is strongly related to the soil type [*Shao et al.*, 2003]. Since our aim is to investigate the location of the most frequent sources of dust emissions, our results will only focus on the dust emission frequencies. The dust emission frequency represents the number of times the wind velocity exceeds the erosion threshold. It can be estimated by combining the erosion threshold map derived from the Z_0 map and meteorological factors, especially surface wind fields. Since soil moisture and snow cover are likely to affect dust emissions in eastern Asia [*Kurosaki and Mikami*, 2004], their influence on the erosion threshold and on dust emission frequencies has been taken into account.

4.1. Method

4.1.1. Erosion Threshold

4.1.1.1. Roughness Length and 10 m Threshold Wind Velocities

[34] *Marticorena and Bergametti* [1995] proposed a parameterization of the threshold wind friction velocity, U_t^* on the basis of a drag partition scheme between the erodible and nonerodible elements present on the surface. This partition depends on the size of the in-place erodible aggregates and is characterized by a smooth roughness length (z_{0s}) and by the roughness length of the surface (Z_0):

$$U_t^*(D_p, Z_0, z_{0s}) = \frac{U_t^*(D_p)}{f_{eff}(Z_0, z_{0s})} \quad (4)$$

where D_p is the soil particle diameter and f_{eff} is the fraction of the total wind shear stress acting on the erodible part of the surface, i.e., the fraction efficient for wind erosion:

$$f_{eff}(Z_0, z_{0s}) = 1 - \left(\frac{\ln\left(\frac{Z_0}{z_{0s}}\right)}{\ln\left(0.35\left(\frac{10}{z_{0s}}\right)^{0.8}\right)} \right)$$

D_p, Z_0 and z_{0s} having units of centimeters.

[35] This parameterization of U_t^* was found to satisfyingly reproduce the erosion threshold wind friction velocities measured in wind tunnels on various natural surfaces whose roughness lengths range from smooth erodible surfaces to rough surfaces strongly protected from erosion [*Marticorena et al.*, 1997b].

[36] This parameterization can be used to assess the erosion threshold wind velocities over the Chinese and Gobi deserts using the Z_0 map derived from PC and an estimation of z_{0s}. *Marticorena and Bergametti* [1995] have tested the sensitivity of the partition scheme to z_{0s}. They found that a standard value of 10^{-3} cm instead of z_{0s} varying from 10^{-4} to 3×10^{-3}cm can be used to reproduce the drag partition with a reasonable confidence level. Thus this value has been used in the present study as standard z_{0s}, except when Z_0 derived from the PC map was lower. In this case, the surface is considered as a smooth bare surface and no drag partition scheme is applied.

[37] In order to provide erosion thresholds easily comparable with wind velocity, we assumed a neutral logarithmic wind profile and compute the 10 m threshold wind velocities, U_t (10 m), corresponding to the threshold wind friction velocities (Figure 6).

[38] The lowest threshold wind velocities ($\sim$7 m s^{-1}) are located in the deserts of the Taklimakan, of Badain Jaran, and of Tengger. However, the threshold distribution over these three deserts differs significantly. In the Taklimakan

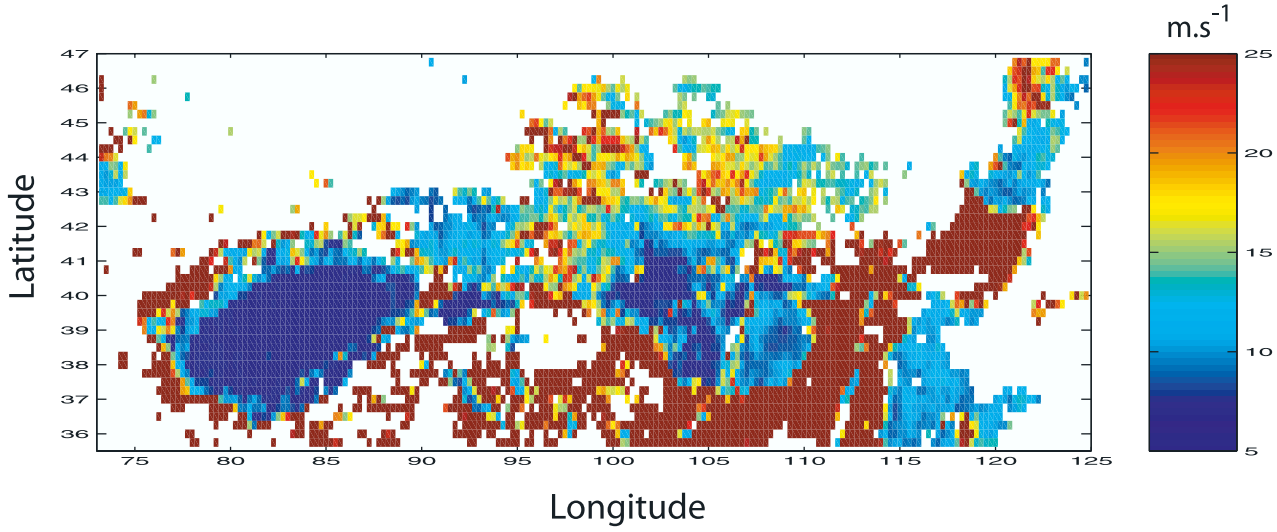

Figure 6. Map of the 10-m erosion threshold wind velocity over the studied area with a spatial resolution of ¼° × ¼°.

desert, the median U_t (10 m) is 7.4 m s^{-1} and a slightly higher value is obtained for the Tengger desert (7.8 m s^{-1}). In the Badan Jarain desert, the median U_t (10 m) is higher (~8.3 m s^{-1}) but 30% of the values are lower than 7.5 m s^{-1}. The erosion threshold are significantly higher in the Mu Us and Horqin sandy lands: in the Mu Us sandy land, the median U_t (10 m) is 9.9 m s^{-1} with a minimum of 7.1 m s^{-1}, and 87% of the values below 13 m s^{-1}; the values obtained for the Horqin sandy land mainly spread between 8.9 and 19 m s^{-1}, with a median U_t (10 m) of 12.2 m s^{-1}. In the Gobi desert, the median U_t (10 m) is 15.4 m s^{-1}, with a minimum of 8.3 m s^{-1}; 90% of the U_t (10 m) values are lower than 20 m s^{-1}. Therefore the dust emission ability of the stony desert will strongly depend on the occurrence of very high surface wind velocities. Threshold wind velocities higher than 25 m s^{-1} are observed in the surrounding mountains of the Taklimakan desert and in the south (35.5°N–37°N and 100°E–110°E) and east (35.5°N–41°N and 110°E–115°E; and 40.5°N–42.5°N and 115°E–120°E) of the northern deserts. Such thresholds should prevent these areas from dust emissions by aeolian erosion.

[39] These simulated erosion thresholds appear consistent with the few available observations of erosion thresholds over Asian deserts. Wind tunnel and field studies in the Gobi desert indicate that the erosion thresholds range from 10 to 12 m s^{-1} [*Murayama*, 1988; *Hu and Qu*, 1997]. The wind velocities measured by the meteorological stations during dust storms also provide an indication of the erosion threshold. *Natsagdorj et al.* [2003] indicated that in Mongolia, dust storms are associated to wind velocities usually ranging from 11 to 20 m s^{-1}. *Wang et al.* [2003] mentioned a minimum wind velocity of 10 m s^{-1} associated with dust storm in the Turpan basin, and between 6 and 8 m s^{-1} in the Tarim basin (i.e., the Taklimakan desert), with a minimum in the southern part of the basin.

4.1.1.2. Soil Moisture and Snow Cover Influence

[40] A parameterization of the influence of the soil moisture on the erosion threshold has been proposed by *Fécan et al.* [1999]. It allowed the computation of the increase of the erosion threshold in wet conditions in reference to dry conditions as a function of the gravimetric soil moisture, w, and of the residual soil moisture, w':

$$\frac{U^*_{tw}}{U^*_{td}} = 1 \quad w < w' \tag{5}$$

$$\frac{U^*_{tw}}{U^*_{td}} = \left[1 + 1.21(w - w')^{0.68}\right]^{0.5} \quad w > w' \tag{6}$$

with w' defined as a function of the soil clay content:

$$w' = 0.0014(\%\ \text{clay})^2 + 0.17(\%\ \text{clay}) \tag{7}$$

w and w' having units of percent (mass of water/mass of dry soil).

[41] The residual moisture w' is the soil water content that must be reached before increasing the erosion threshold [*Fécan et al.*, 1999]. Since the residual soil moisture is parameterized as a function of the soil clay content (equation 7), we used the 1° × 1° soil texture map from FAO [*Zobler*, 1986] to estimate this parameter. Over the studied area, 95% of the computed w' are lower than 10%, but in the desert areas, they are lower than 5%, with a typical value of 0.9% for the sandiest soil.

[42] The soil moisture has been computed using a water balance model including a 2 cm depth surface layer [*Mougin et al.*, 1995]. The model was adapted to include all the soil layers specified in the FAO soil texture profiles [*Webb et al.*, 2000], the texture of the 2 cm surface layer being assigned from the one of the first layer. The water distribution within the soil profile is simulated according to a "tipping bucket" scheme: water that penetrates the soil is assumed to fill the consecutive soil layers up to field capacity. The field capacity of the layers is parameterized as a function of their texture (silt + clay content). The soil water content in the surface layer is determined as a balance between the input water from precipitation, the drainage

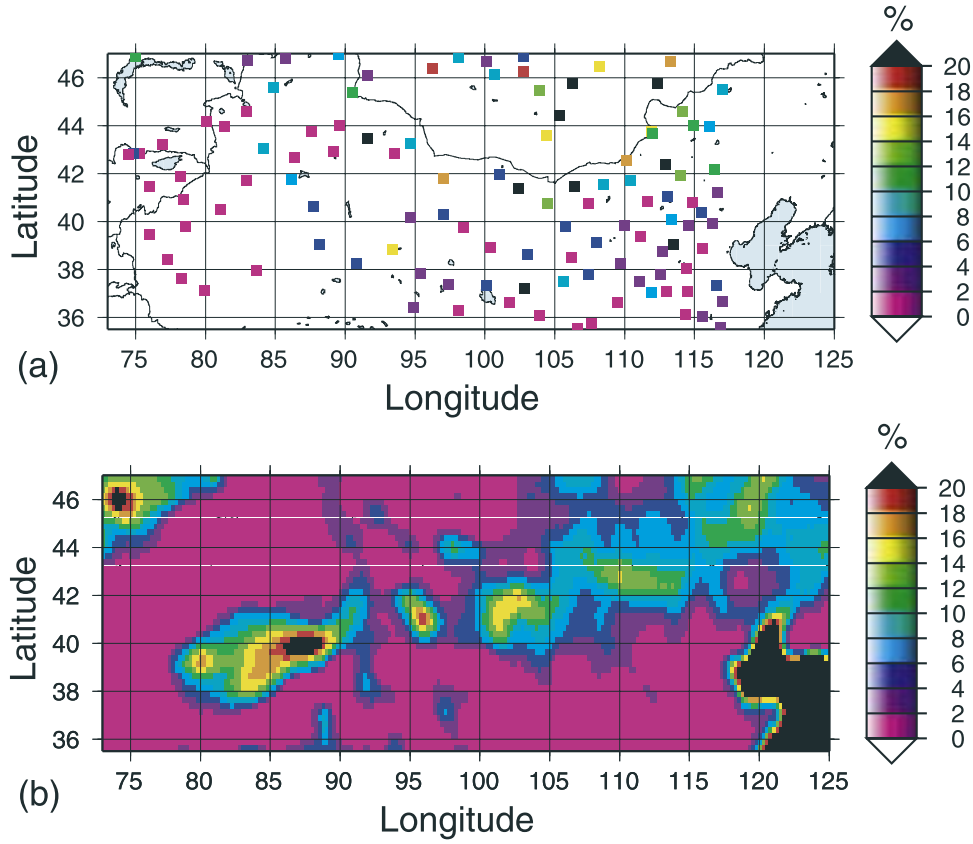

Figure 7. Map of the 1997 annual frequencies of wind velocities >6.5 m s^{-1} (a) measured by the meteorological stations and (b) derived from analyzed ECMWF wind fields.

flux into the next soil layer, and the evapotranspiration (including soil evaporation and plant transpiration). For our simulations, the vegetation cover is forced to 0, and the influence of plant transpiration on the soil water budget is thus neglected. It implies that the simulated soil moisture should be slightly overestimated for permanently vegetated pixels.

[43] The influence of snow cover on the dust emission frequency has been accounted for. We assume that snow cover inhibits dust emission, by totally protecting the erodible surface from erosion.

4.1.2. Meteorological Data

4.1.2.1. Wind Fields

[44] We used the analyzed surface wind fields from the ECMWF (operational archive) at the spatial resolution of 1° × 1° for 1997, 1998, and 1999. The ECMWF wind fields have been used as meteorological forcing of regional transport to simulate mineral dust transport over eastern Asia [*Wang et al.*, 2000; *Uno et al.*, 2001]. The surface wind fields are instantaneous values of the two horizontal components u and v of the horizontal wind which are defined at 10 m height, for 0000, 0600, 1200, and 1800 UT. The wind velocity norm $(u^2 + v^2)^{1/2}$ has been computed from u and v and interpolated to obtain a wind velocity field at the resolution of ¼° × ¼°. To test the influence of the analyzed surface wind fields on the computation of the dust emission frequencies, we compared the frequencies of ECMWF wind velocities higher than 6.5 m s^{-1} to the frequencies derived from the measurements performed in the meteorological stations located in the studied area. Figure 7 illustrates this comparison for 1997. The spatial patterns of the two data sets are in reasonable agreement, despite the fact that measurements provide a very patchy picture. However, the frequencies of wind velocity >6.5 m s^{-1} derived from ECMWF are significantly lower than those derived from meteorological stations. The highest frequency can reach 50% for the measurements, but only 20% for the ECMWF data set. In particular, the frequencies of wind velocity >6.5 m s^{-1} derived from ECMWF do not exceed 15% in the Gobi desert, while measurements from 7 of the meteorological stations located in Mongolia and Inner Mongolia (China) indicate frequencies higher than 20%. In general, they are underestimated by a factor of two in the northern part of the simulated area (>42°N). A hot spot (>20%) of frequencies of ECMWF wind velocities >6.5 m s^{-1} is obtained in the eastern part of the Taklimakan, with a very strong gradient. There is no meteorological station located in this spot, but the measurements from the stations located in the east of the Tarim basin are in reasonable agreement with the ECMWF frequencies for the corresponding grid mesh. In fact, most of the meteorological stations in the Tarim basin are located down the slope of the Kulun Mounts, where ECMWF wind fields exhibit a strong gradient in a very short distance, making the comparison difficult. However, in the Taklimakan desert, both the frequencies of wind velocity >6.5 m s^{-1} derived from measurements and those derived from ECMWF for these stations do not exceed 14%. Finally,

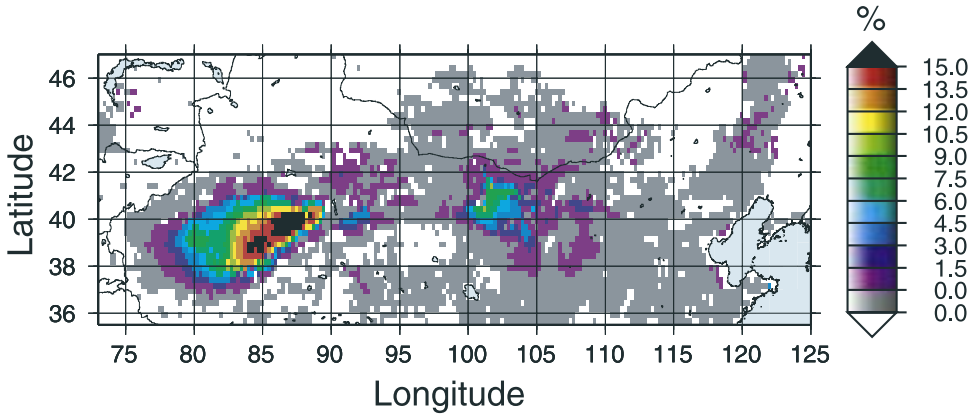

Figure 8. Map of the simulated annual dust emission frequencies averaged on 3 years (1997–1999). (White indicates no simulation, and gray indicates simulated frequency of 0.)

regarding the difference in the spatial scale of the two data sets, we can conclude that the ECMWF surface wind fields reasonably reproduce the observed frequencies of wind velocity >6.5 m s^{-1}, except for the Gobi desert region.

4.1.2.2. Precipitation and Snow Depth

[45] The input data required for the soil moisture computation are: the albedo, the altitude, the daily minimum and maximum surface temperature, and the daily precipitation. We used the data sets from ECMWF (operational archive) with a spatial resolution of 1° × 1°. However, precipitation is the critical parameter for the soil moisture computation.

[46] The distribution of the annual precipitation derived from ECMWF for 1997, 1998 and 1999 reproduces the general trends of the climatology proposed by *Hseung* [1986], the precipitation rates for 1998 being slightly higher than those of the two other years. The daily precipitation fields from ECMWF have been compared with precipitation measured in the meteorological stations located in the studied area. The annual number of days with precipitation observed in the meteorological stations is reasonably reproduced by the ECMWF field (for the 3 years, r ranges from 0.55 to 0.60, n (number of data) from 130 to 133, i.e., probability >99%, and the slope is contained between 1.14 and 1.39). In the Taklimakan desert, the correlation is also significant (r ranges from 0.77 to 0.82, n from 18 to 19, i.e., probability >99%), but the number of days with precipitation is overpredicted within a factor of 2.5 to 3. The scores of agreement between the 6-hour predicted and observed occurrence of precipitation (including coinciding precipitation events and no-precipitation events) computed for each meteorological station are always higher than 75%.

[47] The precipitation rates measured at each time step (6 hours) are not satisfyingly reproduced, in particular for the highest precipitation rates, which can be explained by differences in the spatial scale. When comparing the precipitation rates averaged on regularly spaced precipitation rates classes (57 classes from 0 to 1000 mm), a correct correlation is obtained on a logarithmic scale (r = 0.66, n = 57, i.e., probability >99%, slope = 0.79) suggesting that the variation of the order of magnitude in space and time are reasonably reproduced.

[48] This discrepancy between simulated and observed precipitation rate may not affect significantly the soil moisture in the surface layer, which is the most important layer for the dust emissions. Indeed, because of the tipping bucket principle of the water balance model, the simulation of the soil moisture in the surface layer is more sensitive to the precipitation frequency and to the soil type than to the precipitation rate. However, improvements in the precipitation fields are required to better assess dust emissions, especially in semiarid areas.

[49] The accuracy of the simulated soil moistures is very difficult to assess because of the lack of experimental data. However, the simulated gravimetric soil moistures are in the same order of magnitude than the ones measured and simulated 10-day average volumetric moisture content reported by *Gong et al.* [2003] for April 2001 (0–30% for the simulation, 0–9% for the measurements).

[50] To account for the snow cover, we used the daily snow depth provided by ECMWF (operational archive) at the resolution of 1° × 1°. We assumed that no dust emission occurs when snow was present on the surface (i.e., snow depth >0).

4.1.3. Dust Emission Frequencies

[51] Combining the erosion threshold wind velocity map with the soil moisture fields, the snow cover, and the surface wind fields, the dust emission frequencies over the Chinese and Gobi deserts are estimated. Practically, the erosion threshold is computed daily on the basis of the erosion threshold map derived from POLDER-1 surface products multiplied by the factor of increase due to soil moisture. If the surface wind velocity exceeds the erosion threshold and if snow depth is equal to 0, a dust emission event is simulated. We computed the dust emission frequencies for the years 1997, 1998, and 1999 with a 6-hour time step.

4.2. Results

4.2.1. Location of the Most Frequent Dust Sources

[52] Figure 8 presents annual dust emission frequencies averaged over the 3 simulated years. Two main areas appear as the most frequent sources of dust emissions. The Taklimakan desert exhibits the highest frequencies, which can reach 15 to 19% in the eastern part. The second main area of high dust emission frequencies corresponds to the northern deserts of China, with a maximum frequency of the order of 10% in the Badain Jaran desert, and lower frequencies in the Tengger, the Ulan Buh and the Qubqi deserts (<4%). In the Gobi desert, because of high erosion threshold, the simu-

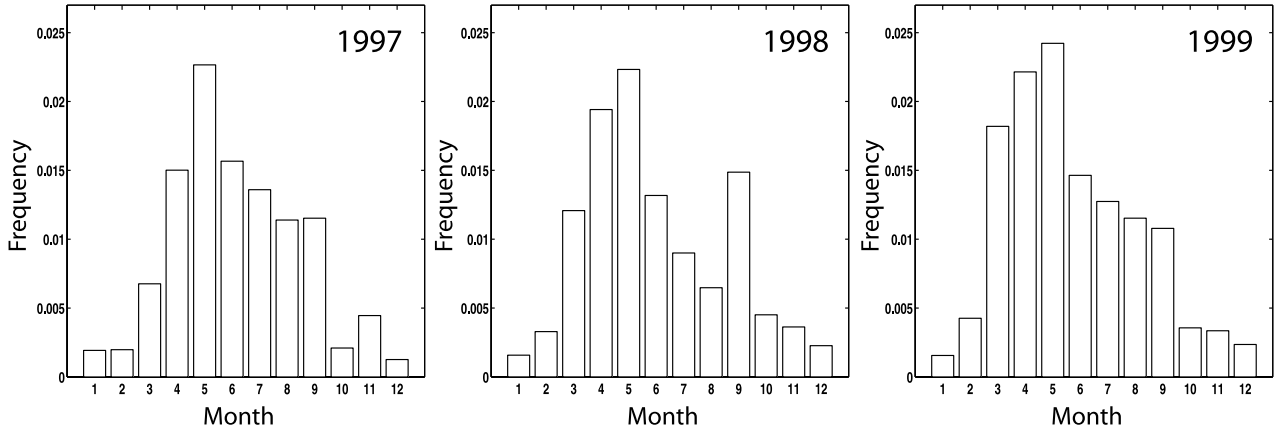

Figure 9. Monthly dust emission frequencies averaged over the whole studied area for 1997, 1998, and 1999.

lated frequencies of dust emissions are very low (<2%) and only correspond to episodes of very high wind velocities. Comparable low dust emission frequencies are simulated over the vegetated Horqin sandy land, suggesting that occasional dust storm can be produced over this region. Low dust emission frequencies simulated in coastal places were either due to sandy surfaces or to a bias in the PC retrieval over irrigated or cultivated surfaces (rice fields, for example). Additional selection criterion should be add in the PC selection to test the relevance of these data, and possibly to exclude them from the composition.

4.2.2. Seasonality of Dust Emissions

[53] Figure 9 presents the monthly dust emission frequencies over the whole area for each of the 3 simulated years.

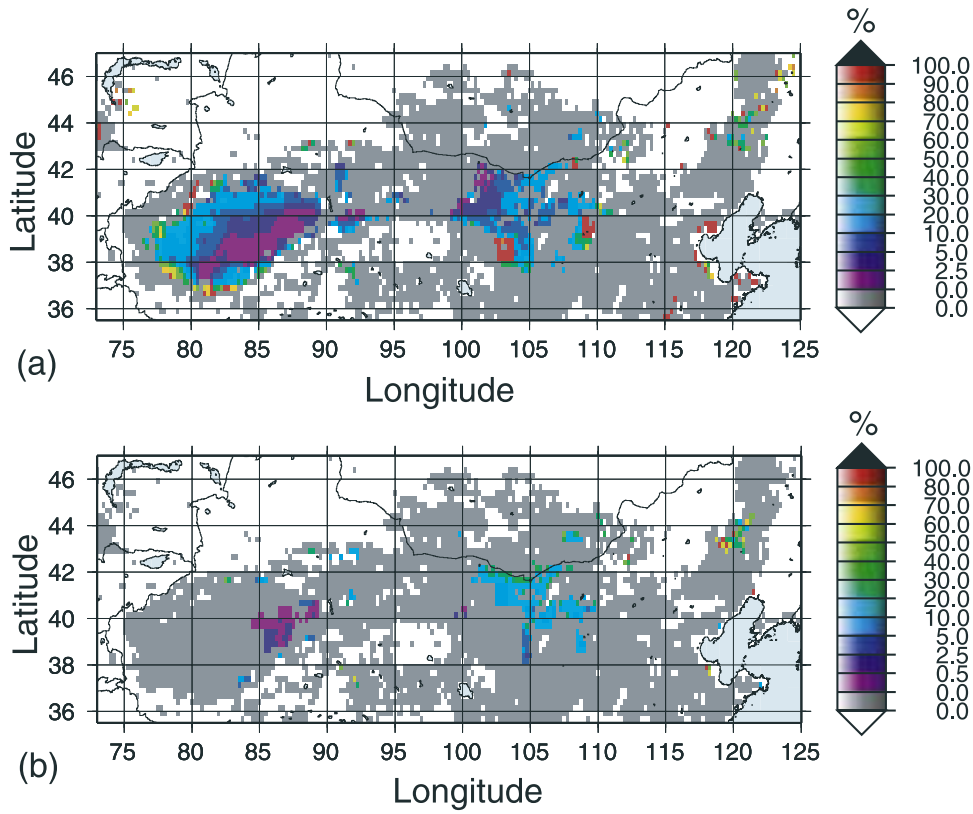

Figure 10. (a) Map of the relative difference between the simulated dust emission frequencies averaged on 3 years (1997–1999) with (wet) and without (dry) accounting for the effect of the soil moisture on the erosion threshold. (b) Map of the relative difference between the simulated dust emission frequencies averaged on 3 years (1997–1999) with accounting for the effect of the soil moisture on the erosion threshold (wet) and with accounting for the effect of the soil moisture and snow cover (complete) on the erosion threshold. (White indicates no simulation, and gray indicates simulated frequency of 0.)

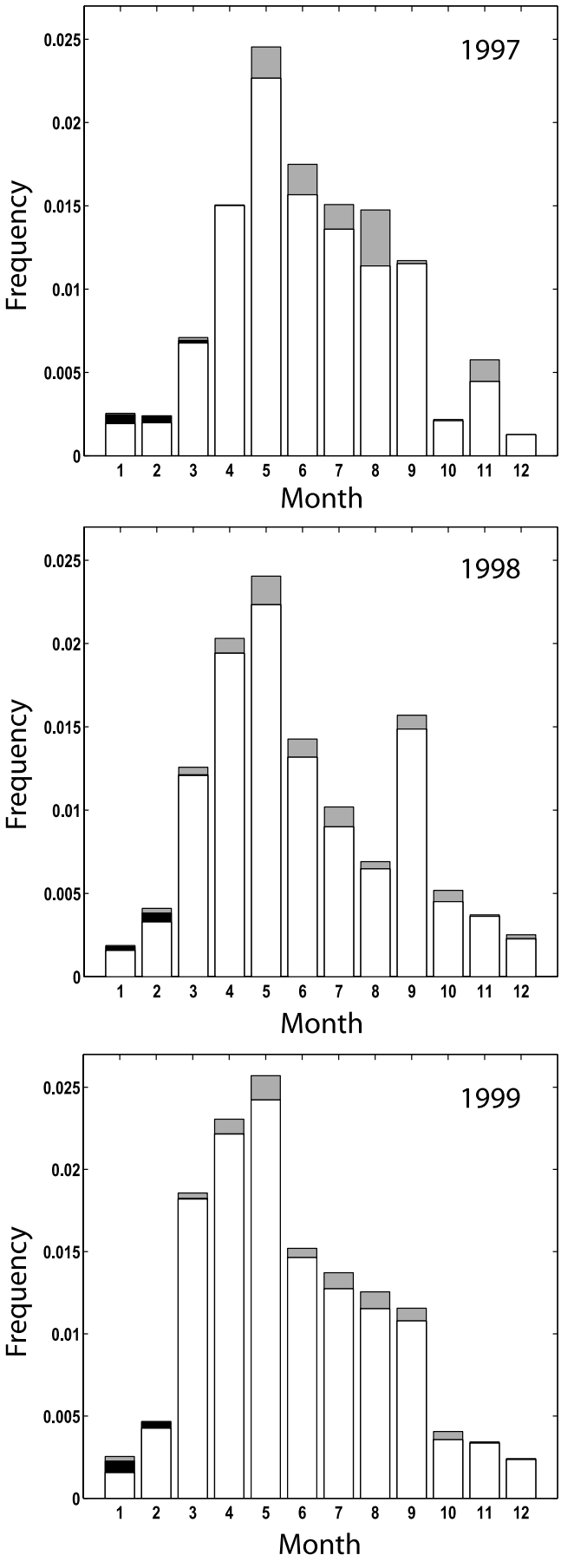

The seasonal cycle is characterized by a maximum in the late spring (April and May) and very low dust emission frequencies in the late autumn and in winter. Such a seasonal cycle is consistent with the general characteristics of the Chinese dust emissions as reported in the literature [*Parungo et al.*, 1994; *Sun et al.*, 2001, 2003]. In 1998 and 1999, the seasonal cycle is very pronounced, with a sharp peak of dust emission frequencies in spring. In 1997, the seasonal cycle is less pronounced: the dust emission frequencies are lower in March and April, but higher in the summer. Some departures from the general trend of the seasonal cycle can be also noticed in November 1997 and in September 1998, with higher dust emission frequencies compared to the same months of the two other years.

4.2.3. Influence of the Soil Moisture and the Snow Cover

[54] We assessed the influence of the soil moisture and of the snow cover on the dust emission frequencies by comparing the "dry" (w = 0 and snow = 0), the "wet" (w = f(time), snow = 0) and the "complete" (w = f(time), snow = f(time)) simulated dust emission frequencies.

[55] Figure 10a reports the relative difference in the dust emission frequencies averaged over the 3 years between dry and wet simulations. The effect of the soil moisture on the dust emission frequencies can be locally important. It globally increases from the southwest to the northeast direction, following the precipitation gradient. In the Taklimakan, the relative difference between the dry and wet frequencies is generally lower than 10%, but can reach 30% in the western and northern parts. It exceeds 70% for groups of pixels located in the borders of the basin. The relative difference between the dry and wet frequencies is generally lower than 10% in the Badain Jaran, can reach 30% in the Ulan Buh, and 70–100% in the Tengger, the southern Qubqi and the northern Badain Jaran deserts. In the Horqin sandy land, the differences range from 70% to 100%. For few isolated pixels in the south of Beijing and near the coast, and close to the Balkhach lake the differences are very important, of the order of 90–100%.

[56] The relative difference between the wet and complete dust emission frequencies averaged over the 3 years (Figure 10b) illustrates the snow cover influence. Figure 10b clearly suggests that the snow cover has less influence than the soil moisture on the dust emission frequencies. The relative difference between the wet and complete frequencies can reach 80–100% for few pixels in the Horqin sandy land and in the Inner Mongolia. In the Horqin sandy land, the differences range globally from 30% to 70%. The relative difference between the wet and complete frequencies is generally included between 5% and 20% in the Ulan Buh, Qubqi, the eastern Tengger and Mu Us, and the northern Badain Jaran deserts, and can reach 70% in the north of the Ulan Buh desert. For a small area in the eastern Gobi desert the differences range from 10% to 20%. In the Taklimakan

Figure 11. Monthly dust emission frequencies averaged over the whole area for 1997, 1998, and 1999 without accounting for the effect of soil moisture and snow cover on the erosion threshold (dry, gray), with accounting for soil moisture only (wet, black) and with accounting for both soil moisture and snow cover (complete, white).

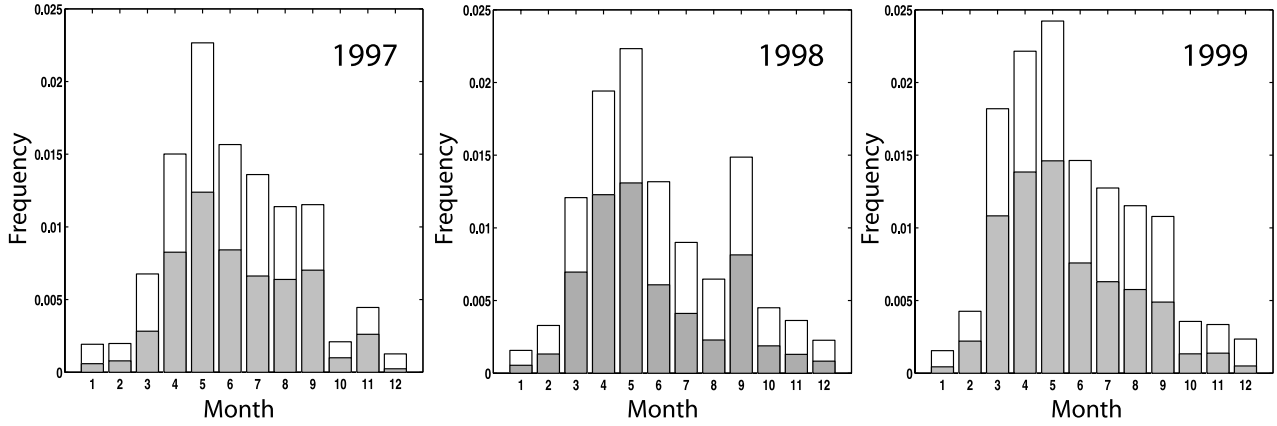

Figure 12. Monthly frequencies of total simulated dust emissions (white) and of significant simulated dust emissions (dust flux $>10^{-10}$ g cm^{-2} s^{-1}) (gray) for 1997, 1998, and 1999 over the whole studied area.

desert, only the eastern part presents differences which are generally lower than 0.5% and reach 2.5% at the maximum.

[57] The influence of the soil moisture and of the snow cover on the seasonal cycle is relatively low for the 3 studied years, as illustrated by Figure 11 reporting the dry, the wet, and the complete monthly dust emission frequencies averaged over the whole area. Soil moisture is mainly noticeable in the spring, in the summer, and in November 1997, but the differences in the monthly dust emission frequencies are always lower than 20%. The snow cover influences the dust emission frequencies only in winter and spring. The influence of snow cover can reach 60% for the whole area (January 1999), but in average, the difference in the dust emission frequencies due to snow is 17% in the winter. It is only 3% in the spring, when dust emission frequencies are the highest. It must be noticed that for the studied years, the influence of the soil moisture and of the snow cover does not vary much from one year to the other.

[58] Our results thus suggest that the influence of soil moisture (and thus precipitation) and snow cover is not sufficient to inhibit the main source areas, or to significantly change the relative intensity of the various deserts in terms of dust emission frequency. The location of the most frequent dust emission sources and their relative importance is thus controlled by the spatial variability of the erosion threshold wind velocity and the frequency of wind velocity higher than these thresholds. Moreover, soil moisture and snow cover are not the main factors controlling the seasonal cycle and the interannual variability of the dust emission frequencies over the Chinese and Gobi deserts. The seasonal cycle and interannual variability of the simulated dust emission frequencies appear as mainly controlled by the variability of the surface wind velocities.

4.2.4. Significant Dust Emission Frequencies

[59] One limitation of the dust emission frequency computation as performed above is that a 10 m wind velocity slightly higher than the erosion threshold wind velocity is automatically considered as a dust emission, i.e., all the dust emissions are considered equally, whatever their intensities. To select only significant dust emissions, a rough estimation of the dust flux has been performed assuming a uniform standard soil size distribution (corresponding to fine sand: D_{med} = 210 μm as by *Marticorena et al.* [1997a]) over the whole area. This approach is not precise enough to compute the dust fluxes but sufficient to define a dust flux threshold in order to select only the significant dust emissions. Dust flux measurements available in the literature range between 10^{-12} and 10^{-5} g cm^{-2} s^{-1}, most of the values ranging between 10^{-9} and 10^{-8} g cm^{-2} s^{-1} [*Marticorena et al.*, 1997a]. Dust flux measurements performed during and out of emission periods in Mali [*Nickling and Gillies*, 1993] provide an estimation of the minimum vertical dust flux measured in background conditions in source regions. From these measurements, it can be assumed that dust fluxes of the order of 10^{-10} g cm^{-2} s^{-1} can unambiguously be considered as significant dust emission fluxes.

[60] Figure 12 represents the distribution of the monthly dust emission frequencies using no threshold or one of 10^{-10} g cm^{-2} s^{-1} on the dust flux, i.e., the total dust emission frequencies and the frequencies of significant dust emissions. The frequencies globally decrease by more than 33% in spring and summer and more than 50% in autumn and winter for the 3 studied years when a 10^{-10} g cm^{-2} s^{-1} threshold is applied on the dust flux. This result indicates that, in average, the dust emissions are probably more intense in spring and summer than in autumn and winter. However, the seasonal cycle and the interannual variability of the significant dust emission frequency are very similar to the ones obtained for the total dust emission frequency.

4.3. Discussion

4.3.1. Location of the Most Frequent Dust Emission Sources

[61] Direct observations of dust storms reported by meteorological stations on synoptic reports have been widely used to establish the climatology of dust emissions in arid and semiarid regions. For example, *Goudie* [1983] used dust storm observations to investigate their distribution in space and time. In northeastern Asia, he identified the Taklimakan desert as the most frequent source of dust storms, with 33 dust storms per year, and the northern deserts of China as the second source with a maximum of 19 dust storms in the Badain Jaran desert. On the basis of the analysis of 40 years (1960–1999) of synoptic observa-

tions from 174 stations located in China and Mongolia, *Sun et al.* [2001] identified the region with the higher dust storm frequency as the region including the southern Gobi desert of Mongolia and China, the Badain Jaran, Tengger, Ulan Buh, Qubqi and Mu Us deserts, and a secondary maximum in the Taklimakan desert. On the basis of a similar time series (1960–2001) of measurements performed in Chinese meteorological stations, *Sun et al.* [2003] confirmed the results from *Goudie* [1983], indicating that the northwestern China, including the Taklimakan, Kumutaq, and Gurban Tonggut, is the region of China where dust storms are the most frequent, and that a secondary region with frequent dust storms is located in central and western part of Inner Mongolia. However, Sun et al. noted that the increase in the number of dust storms, especially observed in spring, during the last years mainly concerns the central and western part of Inner Mongolia. The difference between these two studies can be explained by two factors: (1) *Sun et al.* [2001] focused on the period from March to May, while *Sun et al.* [2003] mentioned that the dust storms frequencies in the Xianjiang Uygur Province, where the Taklimakan is located, are maximum from April to June; (2) both studies are based on interpolation from very sparsely distributed observations, but the study from *Sun et al.* [2001] includes observations in Mongolia, while the study from *Sun et al.* [2003] is restricted to Chinese stations. The inclusion of the Mongolian stations where frequent dust storms (>30 d yr^{-1}) are observed [*Natsagdorj et al.*, 2003] gives more importance to the area of the Gobi and northern deserts. Finally, we can conclude that the two regions where the dust storms are the most frequent are the Taklimakan desert and the Gobi and northern deserts with a comparable importance.

[62] As illustrated in Figure 8, this conclusion is in agreement with the simulated dust emission frequencies which are also the highest in the Taklimakan and the northeastern deserts. The maximum simulated dust emission frequencies for the northern desert are located in the Badain Jaran desert, in agreement with the analyses of the dust storm frequencies in Inner Mongolia [*Gao et al.*, 2003]. However, the extent of the simulated source areas in the northern deserts is not comparable to the one deduced from the interpolated dust storms frequencies including the Mongolian stations. The simulations seem to underestimate the dust emission frequencies in the Gobi desert of Mongolia. This underestimation could be partly explained by the fact that the roughness map is incomplete (50%) over this region but it is more probably related to a bias in the surface wind fields. Indeed the predicted erosion thresholds (8–20 m s^{-1}) are comparable to the wind velocities observed during dust storms in the meteorological stations (11–20 m s^{-1}), but the surface wind velocity almost never exceeds such values in this area. *Husar et al.* [2001] identified two severe dust storms on 15 and 19 April 1998, originating from the Gobi and northern deserts in which surface wind velocities were as high as 20 m s^{-1}. For the less severe dust storm of the two (15 April 1998), our simulations indicate that the erosion thresholds are exceeded over the whole northern deserts where the surface wind velocities are higher than 15 m s^{-1}, but only in a few pixels of the Gobi desert. For the second severe dust storm, the surface wind velocities do not exceed 15 m s^{-1}. They are higher than the erosion thresholds only for a small area of the Gobi desert. It indicates that the ECMWF surface wind velocities are too low to simulate accurately some of the severe dust storms observed in the region of the Gobi and northern deserts.

[63] The simulated dust event frequencies can also be compared to the long-term (1960–2002) simulations of the dust emission from Asian sources performed by *Zhang et al.* [2003] using the dust emission model described by *Gong et al* [2003]. From Zhang et al.'s simulation, ~70% of the Asian dust emissions are produced in the Taklimakan desert, the region including the Badain Jaran, Tengger and Ulan Buh deserts and the Mongolia, with average respective contributions of 21%, 22%, and 29% for the period 1960–2002. However, compared to these averaged contributions, the dust emissions simulated by Zhang et al. for the period from 1995 to 1999 are significantly lower for the Mongolia (~ −40%) and for the region including the Badain Jaran desert (~ −15%), while a very slight increase of the emissions is simulated in the Taklimakan desert. Our results are thus in reasonable agreement with this study for the same period of simulation.

4.3.2. Seasonal and Interannual Patterns

[64] The seasonal cycle derived from synoptic observations is clearly characterized by a maximum in spring with some minor differences depending on the region [*Sun et al.*, 2001; *Gao et al.*, 2003; *Natsagdorj et al.*, 2003; *Sun et al.*, 2003; *Wang et al.*, 2003]. For example, a secondary maximum in the dust storm frequencies can be observed during winter (December and January) in the northern deserts of China or during the fall in some stations of Mongolia or Inner Mongolia [*Gao et al.*, 2003; *Natsagdorj et al.*, 2003; *Sun et al.*, 2003]. The period of maximum dust storm frequencies in the Taklimakan extends from spring to early summer [*Sun et al.*, 2003; *Wang et al.*, 2003]. These two features are well reproduced in our simulations as illustrated in Figure 13.

[65] Finally, the simulated spatial and temporal variations agree with the general features of the dust storms frequencies observed in China and Mongolia. However, very few meteorological stations are located inside the deserts areas, where the maximum dust emission frequencies are simulated limiting the level of confidence of such comparisons. This does not allow any extensive and quantitative comparison. Satellite observations make a quantitative comparison with comparable spatial and temporal scales possible.

4.3.3. Comparison With TOMS Observations

[66] The Aerosol Index (AI) derived from the Earth Probes Total Ozone Mapping Spectrometer (TOMS) is the only available satellite aerosol products over the studied area. A detailed description of the TOMS AI is given by *Herman et al.* [1997] and *Torres et al.* [1998]. The AI relies on the spectral attenuation of the Rayleigh scattering due to aerosol absorption. Positive values generally correspond to UV-absorbing aerosol (e.g., desert dust and carbonaceous particles) while negative values correspond to nonabsorbing aerosols (e.g., sulfate aerosols). The Absorbing Aerosol Index (AAI), defined as the positive values of the AI, has been used to investigate the distribution of the dust sources over the world [*Prospero et al.*, 2002; *Washington et al.*, 2003]. *Washington et al.* [2003] restricted their analysis to positive residues of values greater than 0.7, to avoid contamination by noise resulting from surface signal or nonabsorbing aerosols. However, the TOMS AAI is only a

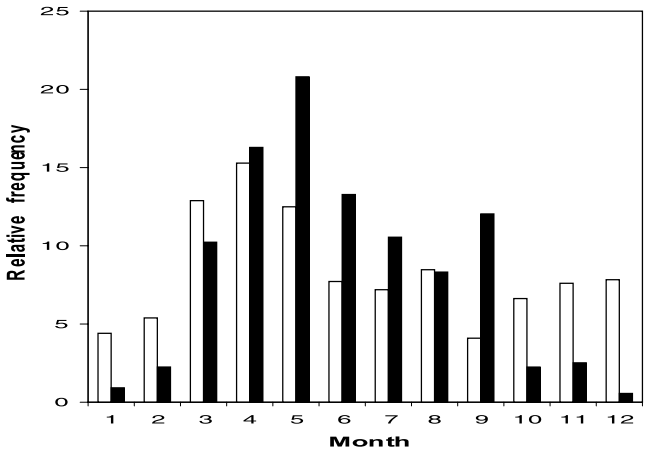

Figure 13. Annual distribution of the relative dust event frequency simulated for 1997–1999 over the Taklimakan (black) and the region including the Gobi desert and the northern deserts of China (white).

semiquantitative indicator of the aerosol atmospheric content. Indeed, it can be influenced by the cloud cover and it is very sensitive to the aerosols layer altitude [*Torres et al.*, 1998; *Chiapello et al.*, 1999; *Hsu et al.*, 1999]. This sensitivity to the aerosol layer altitude makes the discrimination between locally emitted dust and dust transported from remote sources difficult [*Mahowald and Dufresne*, 2004]. However, it is reasonable to assume that the atmospheric load (and thus the TOMS AAI) will be higher close to the region where dust emission occurs, in particular at the TOMS spatial resolution (1° latitude × 1.25° longitude). As a result, we rather expect a relative agreement on the trends of temporal variations at the seasonal and interannual timescales than a quantitative one between the simulated and observed dust emission frequencies.

[67] Daily global data of the Earth Probes TOMS are available in the TOMS website (http://toms.gsfc.nasa.gov/ftpdata.html). From the daily data, following *Washington et al.* [2003], we computed the monthly dust occurrence frequency as the number of TOMS AAI higher than 0.7 related to the total number of observations. Daily observations are missing in November 1997, December 1997, December 1998, and January 1999. For these months, we computed the simulated dust emission frequencies only for the days of available observations.

[68] Figure 14 reports the simulated frequencies of significant dust emissions (Figure 14a) and the frequencies of TOMS AAI > 0.7 (Figure 14b). Both simulations and observations show higher dust emission frequencies in the Taklimakan than in the northern deserts. Moreover, the highest simulated dust emission frequencies (40°N, 87°E) and the highest frequencies of TOMS AAI > 0.7 (40°N, 84°E) are both located in the Taklimakan desert. However, near the south of Beijing eastern coast high frequency of TOMS AAI > 0.7 are observed whereas no dust emissions are simulated over this region, which is not known as a desert or desertified area. Since TOMS AAI is sensitive to UV absorbing aerosols, such high frequencies can be

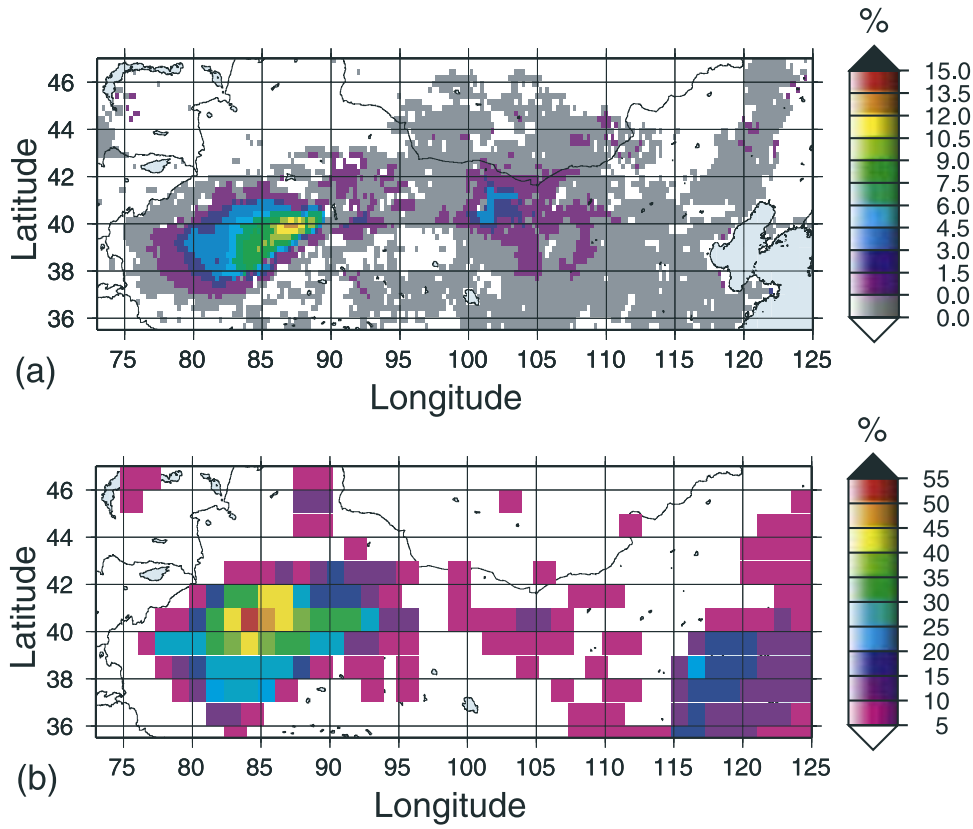

Figure 14. (a) Map of the annual frequencies of significant dust emissions (dust flux $>10^{-10}$ g cm^{-2} s^{-1}) and (b) map of the annual frequencies of TOMS AAI > 0.7 averaged on 3 years (1997–1999).

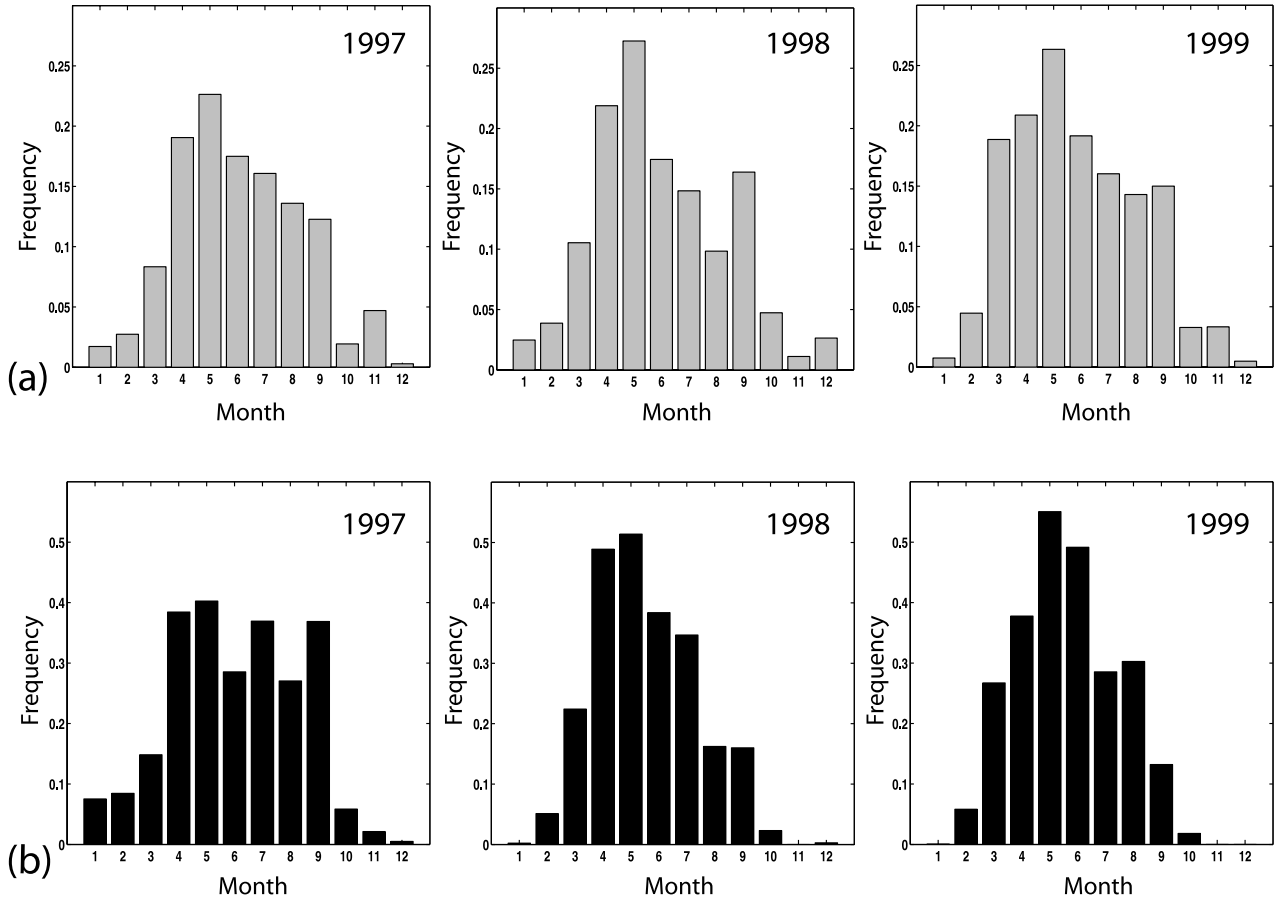

Figure 15. Monthly frequency (a) of significant simulated dust emissions (dust flux $>10^{-10}$ g cm^{-2} s^{-1}) and (b) of TOMS AAI > 0.7 over the Taklimakan desert for 1997, 1998, and 1999.

attributed to other aerosols types, and presumably to carbonaceous aerosols. Indeed, *Herman et al.* [1997] indicated that from December to April, aerosols resulting from coal burning activities in northern China may be mixed with mineral dust and transported eastward over the Pacific Ocean and the southern portions of Japan. To avoid such intricate situations where there is a mixing with other absorbing aerosols, we focused the comparison on the Taklimakan desert (36°N–42°N; 77.5°E–90°E), where mineral dust is expected to be the dominant absorbing aerosol type contributing to the TOMS AAI.

[69] To obtain a more quantitative comparison between the simulations and the frequencies derived from TOMS AAI, we aggregated our results at the TOMS AAI spatial resolution (1° latitude × 1.25° longitude), i.e., 30 simulated pixels. If one pixel out of the 30 exceeds the erosion threshold, the corresponding TOMS resolution pixel is considered as dusty. TOMS AAI are produced from daily instantaneous observations at ∼1120 LT (i.e., ∼0320 UT), while the simulated dust emission frequencies were initially estimated with a 6-hour time step. We thus considered that if a pixel exceeds the erosion threshold once during the 24h previous to the TOMS observation, the corresponding TOMS resolution pixel is considered as dusty.

[70] Figures 15 represents the distributions of monthly simulated frequencies of significant dust emissions (Figure 15a) and of TOMS AAI (AAI > 0.7) (Figure 15b), averaged in the Taklimakan for 1997, 1998, and 1999. The maxima are globally simulated and observed during the same period, i.e., in late spring from April to May. Both the TOMS AAI and the simulations show a more pronounced seasonal cycle in 1998 and 1999 than in 1997; that is, the frequencies are higher in spring (March, April, and May).

[71] There is a general agreement between the simulated and observed frequencies, except during some months in autumn: for example, in September 1997 the simulated frequencies are proportionally lower than the TOMS AAI frequencies, whereas in September 1998 and September 1999 the simulated frequencies are higher than the TOMS AAI ones.

[72] Figure 16 presents the monthly frequencies derived from our simulations of significant dust emissions averaged over the Taklimakan region as a function of the monthly averaged frequencies of TOMS AAI > 0.7 for the 3 studied years. The two data sets are significantly correlated (r between 0.94 and 0.95) for the 3 tested years, with no significant difference in the slope as a function of the year.

[73] We then examined the correlation between the monthly frequencies of simulated significant dust emissions and the monthly frequencies of TOMS AAI > 0.7 for each pixel (1° latitude × 1.25° longitude) and for the 3 years (Figure 17). The range of frequencies derived from TOMS AAI (from 0 to 97%) has been divided in classes 5% wide.

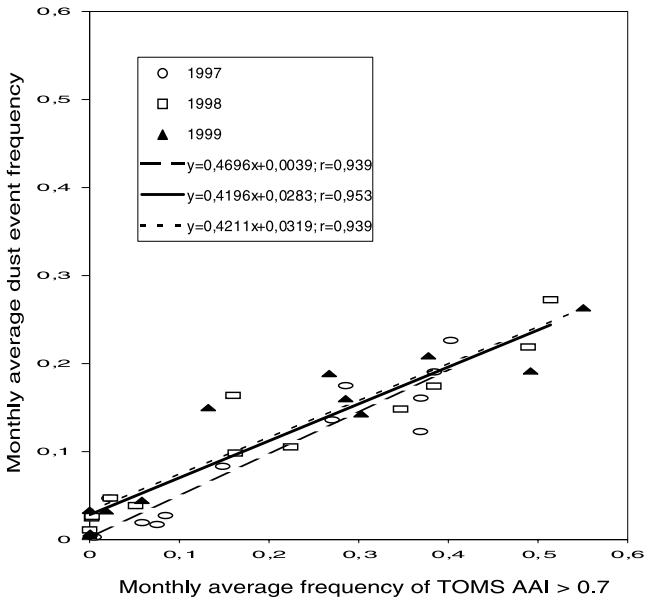

Figure 16. Monthly frequencies of significant simulated dust emissions (dust flux $>10^{-10}$ g cm^{-2} s^{-1}) as a function of the monthly frequencies of TOMS AAI > 0.7 averaged on the Taklimakan desert for 1997, 1998, and 1999.

For each TOMS AAI frequency class, the mean simulated dust emission frequency and the associated standard deviation have been computed. This comparison involved 2160 cases, with a number of tested cases in the different classes varying from 20 to 124, except for the lowest-frequency class (1065 cases), and for the highest one (6 cases), the latter which is not statistically representative. Figure 17 presents the results of this computation for 1997, 1998, and 1999 in the Taklimakan area. We obtain a significant correlation (r = 0.98, slope = 0.44), with similar slope and origin than for the individual pixels. Similar correlations and slopes are obtained on an annual database (1997: r = 0.93, slope = 0.38; 1998: r = 0.98, slope = 0.47; 1999: r = 0.92, slope = 0.38). The simulated dust emission frequencies are systematically lower than those derived from TOMS AAI > 0.7 by a factor from 2 to 2.5. Such a difference may be explained by the fact that both local dust emissions and intense dust plume transported from neighboring pixels can produce high TOMS AAI.

5. Conclusion

[74] In order to describe the influence of the spatial variability of the erosion threshold on the dust emission frequency, we derived a roughness length map over the deserts of China and Mongolia from POLDER-1 surface products. A composition of POLDER-1 PC has been established over the arid and semiarid lands of China and Mongolia (35.5°N–47°N, 73°E–125°E). The composition method includes data selections as a function of the Signal to Noise Ratio (SNR), the number of observations used to derive the BRDF, and of the number of PC values available for individual pixels. This composite map was found consistent with geomorphologic interpretations performed on high-resolution Landsat images and soil properties described in the literature [*Hseung*, 1986; *Walker*, 1986]. The roughness lengths are retrieved from the composite PC on the basis of the empirical relationship established by *Marticorena et al.* [2004]. For the different surface types encountered in the Asian deserts, the retrieved roughness lengths are in agreement with the roughness lengths experimentally determined over similar surface types in other deserts of the world.

[75] From the ¼° × ¼° resolution Z_0 data set, we derived a map of the erosion thresholds expressed as 10 m wind velocities for the Chinese and Gobi deserts. The retrieved erosion thresholds range from 7 up to 20 m s^{-1}, the minimum being located in the sandy deserts (Taklimakan, Badain Jaran, and Tengger deserts) and the maximum in the Gobi desert and the region of the Horqin sandy land. These thresholds are in agreement with the range of minimum wind velocities measured during dust storms in the Taklimakan (6–8 m s^{-1}) [*Wang et al.*, 2003] and in the Gobi desert (11–20 m s^{-1}) [*Natsagdorj et al.*, 2003].

[76] To test the relevance of these erosion thresholds, we computed the dust emission frequencies, i.e., the number of time the wind velocity exceeds the erosion threshold. The computation is performed for 3 years (1997–1998–1999) by combining the 10 m erosion threshold wind velocities, the ECMWF surface wind fields, the snow depth and the soil moisture computed using the FAO soil texture profiles [*Webb et al.*, 2000] and ECMWF meteorological data (precipitation, temperature, etc.).

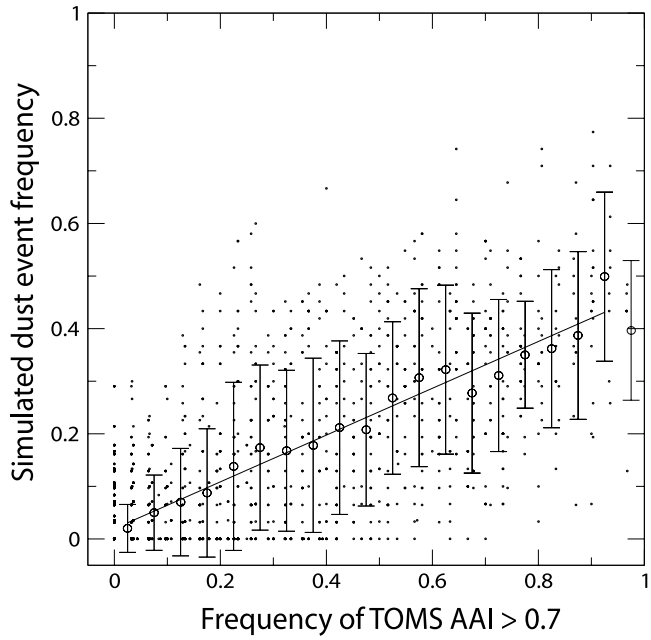

Figure 17. Monthly frequencies of significant simulated dust emissions (dust flux $>10^{-10}$ g cm^{-2} s^{-1}) as a function of the monthly frequencies of TOMS AAI > 0.7 over the Taklimakan desert for the 3 years 1997, 1998, and 1999. Small dots represent individual data; circles represent the averaged frequency of simulated dust emissions for classes (5% width) of frequency of TOMS AAI > 0.7; the solid line represent the linear fit of the averaged data (without accounting for the last class which is not representative).

[77] The sensitivity of the spatial and temporal patterns of the simulated dust emission frequencies to the soil moisture and the snow cover has been investigated. Their influence can locally be important especially in the Horqin Sandy land and in deserts of northern China, but in average the difference in the simulated dust emission frequency due to soil moisture and snow cover does not exceed 20%. These results suggest that soil moisture (and thus precipitation) and snow cover are not the major factors controlling the seasonal cycle and the interannual variability of the dust emission frequencies for the 3 studied years over the Chinese and Gobi deserts. However, a longer period of simulations would be necessary to confirm the reliability of this statement.

[78] From the simulation period (1997–1999), the Taklimakan desert appears as the most frequent source of dust emissions in eastern Asia, with a maximum (15–19%) of dust emission frequencies in the eastern part of the Tarim basin. High dust emission frequencies are also simulated over the deserts of northern China (Badain-Jarain, Tengger, Ulan Buh, Qubqi), the highest simulated frequencies (10%) being located in the Badain Jaran desert. In the Gobi desert, the frequencies of simulated dust emissions are low (<2%) and only occur for very high wind velocity events. The comparison with climatologic studies based on synoptic data [*Goudie*, 1983; *Sun et al.*, 2001; *Gao et al.*, 2003; *Natsagdorj et al.*, 2003; *Sun et al.*, 2003; *Wang et al.*, 2003] confirm these two regions as major dust storm centers. It also reveals an underestimation of the dust emission frequency in the Gobi desert. This underestimation appears as mainly related to a bias in the surface wind fields used for the simulations.

[79] The simulated dust emission frequencies exhibit a clear seasonal cycle with a maximum in the late spring (April and May) and a minimum in late autumn and in winter. The seasonal cycle fully agrees with the seasonal cycle established from synoptic observation of dust storms in the regions of the main source areas [*Sun et al.*, 2001; *Gao et al.*, 2003; *Natsagdorj et al.*, 2003; *Sun et al.*, 2003; *Wang et al.*, 2003]. Some minor features of the seasonal cycle observed in the different source regions, such as the occurrence of a secondary maximum, or the duration of the period of maximum dust emission, are also reproduced by the simulations. A noticeable interannual variability is observed for the 3 studied years, especially during the summer months.

[80] Over the Taklimakan desert, the simulated frequencies of significant dust emissions have been compared to the frequencies of occurrence of TOMS AAI higher than 0.7. Both the location and the relative intensity of the highest dust emission frequencies identified from the simulations are in agreement with the observations. Over the Taklimakan desert, monthly frequencies of significant dust emissions and frequencies of TOMS AAI higher than 0.7 were found to be correlated.

[81] **Acknowledgments.** This work was supported by the French "Programme National de Chimie Atmosphérique" in the framework of the "Aérosols-Climat" project. The results presented in this paper were obtained using data from the Centre National d'Etudes Spatiales (CNES) acquired by POLDER-1 instrument onboard NASDA's ADEOS. The Earth Probe TOMS AI was made available by the NASA/GSFC TOMS Ozone Processing Team (OPT). One time global publication right for the Landsat image was granted by the Earth Satellite Corporation Team. We would like to thank Elisabeth Bon Nguyen for the adaptation of the Chinese map.

References

Alfaro, S. C., and L. Gomes (2001), Modeling mineral aerosol production by wind erosion: Emission intensities and aerosol distributions in source areas, *J. Geophys. Res*, *106*, 18,075–18,084.

Chiapello, I., J. M. Prospero, J. Herman, and C. Hsu (1999), Detection of mineral dust over the North Atlantic Ocean and Africa with the Nimbus 7 TOMS, *J. Geophys. Res.*, *104*, 9277–9291.

Duce, R. A. (1995), Sources, distributions, and fluxes of mineral aerosols and their relationship to climate, in *Aerosol Forcing of Climate*, edited by R. J. Charlson and J. Heintzenberg, pp. 43–72, John Wiley, Hoboken, N. J.

Fécan, F., B. Marticorena, and G. Bergametti (1999), Parameterization of the increase of the aeolian erosion threshold wind friction due to soil moisture for semi arid areas, *Ann. Geophys.*, *17*, 149–157.

Gao, T., X. Yu, Q. Ma, H. Li, X. Li, and Y. Si (2003), Climatology and trends of the temporal and spatial distribution of sandstorms in Inner Mongolia, *Water Air Soil Pollut.*, *3*, 51–66.

Gillette, D. A., J. Adams, D. R. Muhs, and R. Khil (1982), Threshold friction velocities and rupture moduli for crusted desert soils for the input of soil particles into the air, *J. Geophys. Res.*, *87*, 9003–9015.

Gong, S. L., X. Y. Zhang, T. L. Zhao, I. G. McKendry, D. A. Jaffe, and N. M. Lu (2003), Characterization of soil dust aerosol in China and its transport and distribution during 2001 ACE-Asia: 2. Model simulation and validation, *J. Geophys. Res.*, *108*(D9), 4262, doi:10.1029/2002JD002633.

Goudie, A. S. (1983), Dust storms in space and time, *Prog. Phys. Geog.*, *7*, 502–530.

Greeley, R., and J. D. Iversen (1985), *Wind as a Geological Process*, Cambridge Univ. Press, New York.

Greeley, R., D. G. Blumberg, J. F. McHone, A. Dobrovolski, J. Iversen, N. Lancaster, K. R. Rasmussen, S. Wall, and B. White (1997), Applications of spaceborne radar laboratory data to the study of aeolian processes, *J. Geophys. Res.*, *102*, 10,971–10,983.

Hautecoeur, O., and M. Leroy (1998), Surface bidirectional reflectance distribution function observed at global scale by POLDER/ADEOS, *Geophys. Res. Lett.*, *25*, 4197–4200.

Herman, J. R., P. K. Bhartia, O. Torres, C. Hsu, C. Seftor, and E. Celarier (1997), Global distribution of UV-absorbing aerosols from Nimbus 7/TOMS data, *J. Geophys. Res.*, *102*, 16,911–16,922.

Hseung, Y. (1986), *The Soil Atlas of China*, Cartogr. Publ., Beijing.

Hsu, N. C., J. R. Herman, O. Torres, B. N. Holben, D. Tanre, T. F. Eck, A. Smirnov, B. Chatenet, and F. Lavenu (1999), Comparisons of the TOMS aerosol index with Sun-photometer aerosol optical thickness: Results and applications, *J. Geophys. Res.*, *104*, 6269–6279.

Hu, M. C., and J. Z. Qu (1997), Preliminary estimate of dust deflation amount in Hexi Corridor, Gansu province, in *Dust Storm Studies in China*, pp. 118–120, Chin. Meteorol. Press, Beijing.

Husar, R. B., et al. (2001), Asian dust events of April 1998, *J. Geophys. Res*, *106*, 18,317–18,330.

Intergovernmental Panel on Climate Change (2001), *Climate Change 2001: The Scientific Basis. Contribution of Working Group 1 to the Third Assessment Report of the Intergovernmental Panel on Climate Change*, Cambridge Univ. Press, New York.

Kurosaki, Y., and M. Mikami (2003), Recent frequent dust events and their relation to surface wind in east Asia, *Geophys. Res. Lett.*, *30*(14), 1736, doi:10.1029/2003GL017261.

Kurosaki, Y., and M. Mikami (2004), Effect of snow cover on threshold wind velocity of dust outbreak, *Geophys. Res. Lett.*, *31*, L03106, doi:10.1029/2003GL018632.

Leroy, M., J. L. Deuzé, F. M. Bréon, O. Hautecoeur, M. Herman, J. C. Buriez, D. Tanré, S. Bouffiès, P. Chazette, and J. L. Roujean (1997), Retrieval of atmospheric properties and surface bidirectional reflectances over land from POLDER/ADEOS, *J. Geophys. Res.*, *102*, 17,023–17,039.

Li, L., and L. W. Martz (1994), System of numeric models for sand particle transport by wind, *J. Geophys. Res.*, *99*, 12,999–13,012.

Mahowald, N. M., and J. L. Dufresne (2004), Sensitivity of TOMS aerosol index to boundary layer height: Implications for detection of mineral aerosol sources, *Geophys. Res. Lett.*, *31*, L03103, doi:10.1029/2003GL018865.

Mainguet, M. (1996), Aridité, sécheresse et dégradation dans les aires sèches de Chine, *Sécheresse*, *7*, 41–50.

Marticorena, B., and G. Bergametti (1995), Modeling the atmospheric dust cycle: 1. Design of a soil-derived dust emission scheme, *J. Geophys. Res.*, *100*, 16,415–16,430.

Marticorena, B., G. Bergametti, B. Aumont, Y. Callot, C. N'Doumé, and M. Legrand (1997a), Modeling the atmospheric dust cycle: 2. Simulations of Saharan dust sources, *J. Geophys. Res.*, *102*, 4387–4404.

Marticorena, B., G. Bergametti, D. A. Gillette, and J. Belnap (1997b), Factors controlling threshold friction velocity in semiarid and arid areas of the United States, *J. Geophys. Res.*, *102*, 23,277–23,287.

Marticorena, B., P. Chazette, G. Bergametti, F. Dulac, and M. Legrand (2004), Mapping the aerodynamic roughness length of desert surfaces from the POLDER/ADEOS bi-directional reflectance product, *Int. J. Remote Sens.*, *25*, 603–626.

McKenna-Neuman, C., and W. G. Nickling (1994), Momentum extraction with saltation: Implications for experimental evaluation of wind profile parameters, *Boundary Layer Meteorol.*, *68*, 35–50.

Mitchell, D. J., and M. A. Fullen (1994), Soil-forming processes on reclaimed desertified land in north-central China, in *Environmental Change in Drylands: Biogeographical and Geomorphological Perspectives*, edited by A. C. Milington and K. Pye, pp. 393–412, John Wiley, Hoboken, N. J.

Mougin, E., D. Lo Seen, S. Rambal, A. Gaston, and P. Hiernaux (1995), A regional sahelian grassland model to be coupled with multispectral satellite data. I: Model description and validation, *Remote Sens. Environ.*, *52*, 191–193.

Murayama, N. (1988), Dust cloud "Kosa" from the east Asian dust storms in 1982–1988 as observed by GMS satellite, *Meteorol. Satell. Cent. Tech. Note*, *17*, 1–8.

Natsagdorj, L., D. Jugder, and Y. S. Chung (2003), Analysis of dust storms observed in Mongolia during 1937–1999, *Atmos. Environ.*, *37*, 1401–1411.

Nickling, W. G., and J. A. Gillies (1993), Dust emission and transport in Mali, West Africa, *Sedimentology*, *40*, 859–868.

Nickovic, S., G. Kallos, A. Papadopoulos, and O. Kakaliagou (2001), A model for prediction of desert dust cycle in the atmosphere, *J. Geophys. Res.*, *106*, 18,113–18,129.

Parungo, F., Z. Li, X. Li, D. Yang, and J. Harris (1994), Gobi dust storms and the great green wall, *Geophys. Res. Lett.*, *21*, 999–1002.

Prospero, J. M., P. Ginoux, O. Torres, S. E. Nicholson, and T. E. Gill (2002), Environmental characterization of global sources of atmospheric soil dust identified with the Nimbus 7 Total Ozone Mapping Spectrometer (TOMS) absorbing aerosol product, *Rev. Geophys.*, *40*, 1002, doi:10.1029/2000RG000095.

Roujean, J. L. (1991), Modélisation des effets bidirectionnels de la réflectance de surface pour la normalisation de données satellitaires de télédétection, Ph.D. thesis, 172 pp., Univ. Paul Sabatier, Toulouse, France.

Roujean, J. L., M. Leroy, and P. Y. Deschamps (1992), A bidirectional reflectance model of the Earth's surface for the correction of remote sensing data, *J. Geophys. Res.*, *97*, 20,455–20,468.

Roujean, J. L., D. Tanré, F. M. Bréon, and J. L. Deuzé (1997), Retrieval of land surface parameters from airborne POLDER bidirectional reflectance distribution function during HAPEX-Sahel, *J. Geophys. Res.*, *102*, 11,201–11,218.

Shao, Y. (2001), A model for mineral dust emission, *J. Geophys. Res.*, *106*, 20,239–20,254.

Shao, Y., M. R. Raupach, and J. F. Leys (1996), A model for predicting aeolian sand drift and dust entrainment on scales from paddock to region, *Aust. J. Soil Res.*, *34*, 309–342.

Shao, Y., Y. Yang, J. Wang, Z. Song, L. M. Leslie, C. Dong, Z. Zhang, Z. Lin, Y. Kanai, S. Yabuki, and Y. Chun (2003), Northeast Asian dust storms: Real-time numerical prediction and validation, *J. Geophys. Res.*, *108*(D22), 4691, doi:10.1029/2003JD003667.

Sun, J. (2002), Provenance of loess material and formation of loess deposits on the Chinese Loess Plateau, *Earth Planet. Sci. Lett.*, *203*, 845–859.

Sun, J., M. Zhang, and T. Liu (2001), Spatial and temporal characteristics of dust storms in China and its surrounding regions, 1960–1999: Relations to source area and climate, *J. Geophys. Res.*, *106*, 10,325–10,333.

Sun, L., X. Zhou, J. Lu, Y. P. Kim, and Y. S. Chung (2003), Climatology, trend analysis and prediction of sandstorms and their associated dustfall in China, *Water Air Soil Pollut.*, *3*, 41–50.

Tegen, I., M. Werner, S. P. Harrison, and K. E. Kohfeld (2004), Relative importance of climate and land use in determining present and future global soil dust emission, *Geophys. Res. Lett.*, *31*, L05105, doi:10.1029/2003GL019216.

Torres, O., P. K. Bhartia, J. R. Herman, Z. Ahmad, and J. Gleason (1998), Derivation of aerosol properties from satellite measurements of backscattered ultraviolet radiation: Theoretical basis, *J. Geophys. Res.*, *103*, 17,099–17,110.

Uno, I., H. Amano, S. Emori, K. Kinoshita, I. Matsui, and N. Sugimoto (2001), Trans-Pacific yellow sand transport observed in April 1998: A numerical simulation, *J. Geophys. Res.*, *106*, 18,331–18,344.

Walker, A. S. (1986), Eolian landforms, in *Geomorphology From Space: A Global Overview of Regional Landforms*, edited by N. M. Short and R. W. Blair, chapter 8, NASA, Greenbelt, Md.

Wang, X., Y. Ma, H. Chen, G. Wen, S. Chen, Z. Tao, and Y. S. Chung (2003), The relation between sandstorms and strong winds in Xinjiang, China, *Water AirSoil Pollut.*, *3*, 67–79.

Wang, Z., H. Ueda, and M. Huang (2000), A deflation module for use in modeling long-range transport of yellow sand over east Asia, *J. Geophys. Res.*, *105*, 26,947–26,959.

Washington, R., M. Todd, N. J. Middleton, and A. S. Goudie (2003), Dust-storm source areas determined by the Total Ozone Monitoring Spectrometer and surface observations, *Ann. Assoc. Am. Geogr.*, *93*(2), 297–313.

Webb, R. W., C. E. Rosenzweig, and E. R. Levine (2000), Global soil texture and derived water-holding capacities, Oak Ridge Natl. Lab. Distrib. Active Arch. Cent., Oak Ridge, Tenn.

Xue, Y. (1996), The impact of desertification in the Mongolian and the inner Mongolian grassland on the region climate, *J. Clim.*, *9*, 2173–2189.

Zha, Y., and J. Gao (1997), Characteristics of desertification and its rehabilitation in China, *J. Arid Environ.*, *37*, 419–432.

Zhang, X. Y., S. L. Gong, T. L. Zhao, R. Arimoto, Y. Q. Wang, and Z. J. Zhou (2003), Sources of Asian dust and role of climate change versus desertification in Asian dust emission, *Geophys. Res. Lett.*, *30*(24), 2272, doi:10.1029/2003GL018206.

Zobler, L. (1986), A world soil file for global climate modelling, *NASA Tech. Memo., TM-87802*.

G. Bergametti, B. Laurent, B. Marticorena, and C. Schmechtig, LISA, UMR-CNRS 7583, Université PVII/PXII, 61 avenue du général de Gaulle, F-94010 Créteil, France. (bergametti@lisa.univ-paris12.fr; blaurent@lisa.univ-paris12.fr; marticorena@lisa.univ-paris12.fr; schmechtig@lisa.univ-paris12.fr)

P. Chazette and F. Maignan, LSCE, UMR-CNRS 1572, CEA, L'orme des merisiers 709, F-91191 Gif/Yvette Cedex, France. (pch@lsce.saclay.cea.fr; maignan@lsce.saclay.cea.fr)